D4.8 Bornholm Lighthouse UC-4 report

Engelhardt, Jan; Gabderakhmanova, Tatiana; Calearo, Lisa; Zepter, Jan Martin Wilhelm; Ledro, Mirko; Marinelli, Mattia

Publication date:
2021

Document Version
Publisher's PDF, also known as Version of record

D4.8 Bornholm Lighthouse UC-4 report

WP4 – Modelling, simulation, engineering, and equipment development for the Lighthouse demonstration

INSULAE
Maximizing the impact of innovative energy approaches in the EU islands

Grant agreement: 824433

Prepared by Jan Engelhardt, Tatiana Gabderakhmanova, Lisa Calearo, Jan Martin Zepter, Mirko Ledro, Mattia Marinelli (Technical University of Denmark)

Date: 25/06/2021

This project has received funding from the European Union's Horizon 2020 research and innovation programme under Grant Agreement No 824433

DELIVERABLE FACTSHEET

Document Name: Bornholm Lighthouse UC-4 report
Responsible Partner: DTU
WP: WP4 – Modelling, simulation, engineering, and equipment development for the Lighthouse demonstration
Task: T4.3 Bornholm Lighthouse demonstration preparatory activities
Deliverable nº: 4.8

Approvals

Dissemination level	
X	PU = Public
	PP = Restricted to other programme participants (including the EC)
	RE = Restricted to a group specified by the consortium (including the EC)
	CO = Confidential, only for members of the consortium (including the EC)

	Company
Author/s	DTU
Task Leader	DTU
WP Leader	CIRCE

Documents history

Revision	Date	Main modification	Author
1	29/03/2021	Draft version	DTU
2	14/06/2021	First version	DTU
3	25/06/2021	Final version sent to CIRCE	DTU

DISCLAIMER OF WARRANTIES

"This project has received funding from the European Union's Horizon 2020 research and innovation programme under Grant Agreement No 824433".

This document has been prepared by INSULAE project partners as an account of work carried out within the framework of the EC-GA contract no 824433.

Neither Project Coordinator, nor any signatory party of INSULAE Project Consortium Agreement, nor any person acting on behalf of any of them:

(a) makes any warranty or representation whatsoever, express or implied,
  (i). with respect to the use of any information, apparatus, method, process, or similar item disclosed in this document, including merchantability and fitness for a particular purpose, or
  (ii). that such use does not infringe on or interfere with privately owned rights, including any party's intellectual property, or
  (iii). that this document is suitable to any particular user's circumstance; or

(b) assumes responsibility for any damages or other liability whatsoever (including any consequential damages, even if Project Coordinator or any representative of a signatory party of the INSULAE Project Consortium Agreement, has been advised of the possibility of such damages) resulting from your selection or use of this document or any information, apparatus, method, process, or similar item disclosed in this document.

ABBREVIATIONS

BESS	Battery energy storage system
BM	Battery module
BMS	Battery management system
CCS	Combined charging system
CHAdeMO	CHArge de MOve
COM	Crossover module
EMS	Energy management system
EV	Electric vehicle
EV-HPC	High-power electric vehicle charging station
GSH	Green Solution House
HPC	High-power charging station
ILCR	In-line current regulator
KPI	Key performance indicator
LFP	Lithium iron phosphate
MOSFET	Metal-oxide-semiconductor field effect transistor
MPPT	Maximum power point tracking
NSS	Nerve Smart Systems
PV	Photovoltaics
PECS	Power electronic converter system
RES	Renewable energy sources
SCM	String control module
SOC	State-of-charge
SOH	State-of-health
UC-4	Use case 4

EXECUTIVE SUMMARY

Deliverable 4.8 collects main results and conclusions reached after finalizing modelling, engineering, and equipment development activities preceding to the deployment of the equipment in Use case 4.

Use case 4 overarching objective is to demonstrate the operation of a DC microgrid consisting of multiple units. The microgrid is formed by a reconfigurable storage system with an overall energy capacity of 312 kWh, a 61 kW photovoltaic plant, and two 175 kW EV fast charging stations along with a 43 kW connection to the public grid. Detailed objectives of the demonstration focus on assessing the energy management across the different components while minimizing energy losses, increasing therefore the overall system efficiency compared to a traditional system. The capability of the DC microgrid in harvesting more PV production is therefore benchmarked with another identical 61 kW photovoltaic system connected through a traditional DC/AC inverter. Particular focus is given to the specific characterization of the reconfigurable system and its inherent control and optimization, while achieving EV fast charging objectives with locally produced photovoltaic energy and minimal request of power from the public grid.

This deliverable provides a general overview of the use case, final architecture, sizing and operation principle of the DC microgrid, detailed description of its energy components, and the environment it will be integrated in. It also collects an extensive set of results and conclusions based on data-driven simulations focused on testing different energy management and control approaches and functions on the system- and on the battery cell level.

Results collected in this deliverable are based on scientific papers generated as part of the Insulae project and master thesis projects conducted at the Technical University of Denmark.

D4.8 concludes, together with D4.9 (Bornholm Lighthouse Use Case-5 report), the simulation activities in the task T4.3 (Bornholm Lighthouse demonstration preparatory activities) of the INSULAE project.

TABLE OF CONTENTS

LIST OF FIGURES

LIST OF TABLES

1 INTRODUCTION

The renewable energy transition offers the chance for a low carbon, environmentally friendly, and affordable energy supply. Consequently, the electrical sector is in rapid development, as fossil fuels based are being replaced by renewable energy sources. This causes the traditional power system, where the energy production is concentrated in a few and large power plants, to be transformed into a decentralised power system, where producing units such as wind farms and PV systems are integrated on distribution level. However, ensuring stable and reliable grid operation despite the fluctuating and uncontrollable nature of renewables remains one of the main challenges of this transformation. At the same time, the transportation sector is currently experiencing a paradigm shift as gasoline powered vehicles are being gradually replaced with electric vehicles (EVs) [1]-[3]. The integration of EVs in an electricity system with a high share of renewables offers the opportunity for a future mobility with overall reduced greenhouse gas emission. However, the rising number of electric vehicles further increases the total electric load and might eventually lead to congestions and unbalances in the distribution grid. Especially fast-charging processes are impacting the grid, due to the high peak-load demand and the inflexible charging times.

All in all, these developments bring new challenges for the operation of distribution grids and require novel solutions to maintain the stability of the power system. In this context, microgrids are gaining importance, as they enable a safe operation on distribution level and can potentially run without connection to the public grid. DC microgrids could be a feasible solution specifically in use cases where many components are in DC, such as PV systems, stationary battery storage, and electric vehicles. A reduced number of conversion stages might decrease power losses, thus improving the overall efficiency of the power system.

Within the activities of Use Case 4 (UC-4) “Transition to DC grids”, a DC microgrid will be deployed on the Danish island of Bornholm. The demonstration provides the unique opportunity to test the concept in real life [4]. The prototype consists of a PV system as a renewable energy source, a battery energy storage system (BESS), two fast chargers for electric vehicles (EVs), and an inverter as the link to the surrounding AC grid. Figure 1 provides an overview of different perspectives related to the installation. The BESS provides buffering functionality for both PV production and EV consumption [5], [6]. Hence, it allows for using renewable energy locally. Furthermore, the buffering effect enables the EV fast chargers to provide power levels above the capacity of the surrounding AC distribution grid, thus reducing charging times for EV owners significantly. The BESS itself is a novel type of battery that can change its cell topology in a real-time fashion [7], [8]. This provides the battery with the unique capability to adjust its own voltage level during operation, which makes it possible to couple the battery strings directly with other DC components, such as the PV system and EVs. Consequently, no DC-DC converters are required between the units of the DC microgrid. Moreover, the reconfigurability of the storage system allows to operate all battery

cells according to their individual performance. This aims at reducing cell unbalance issues and potentially increase the lifetime of the whole battery system. The inverter serves as the interface to the surrounding AC grid. The combination of BESS and inverter provides the microgrid with peak shaving capability to reduce energy exchange with the AC grid and increase self-consumption. Furthermore, the inverter can be used to provide grid services for the AC grid, such as frequency and voltage control. The energy management system is responsible for planning and controlling the energy level of the BESS, and coordinating the power flow between the different components of the DC microgrid. It aims at optimizing the operation of each component and to minimize degradation of the BESS.

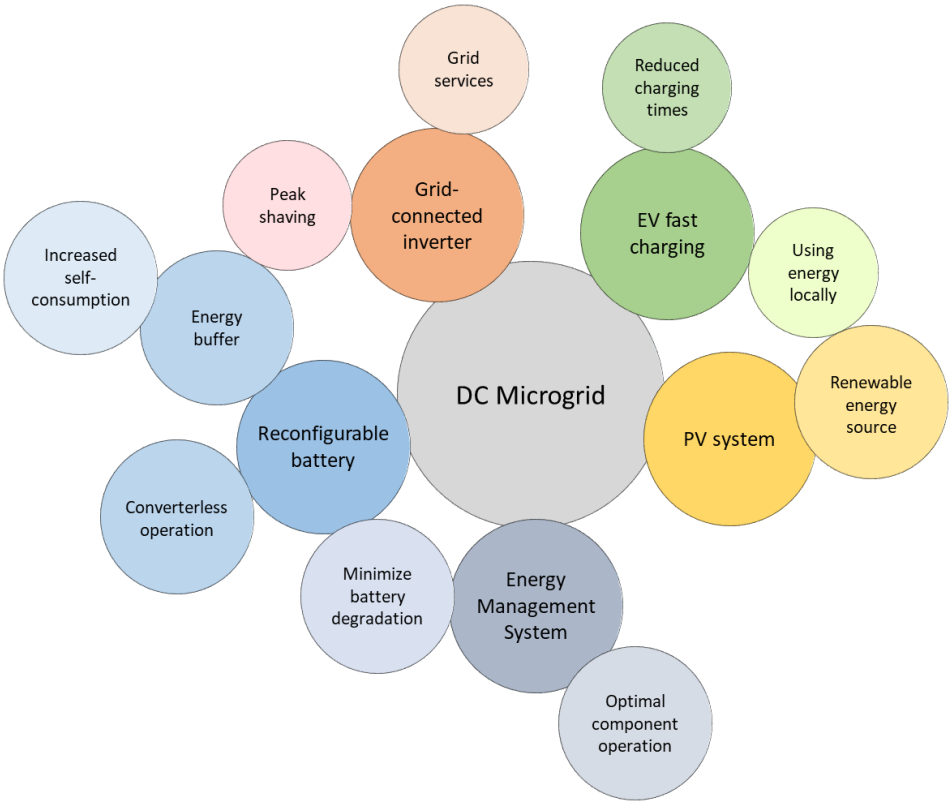

Figure 1: Overview of the scope of possible investigations around the Use Case 4.

Deliverable D4.8 collects main results and conclusions reached after finalizing modelling, engineering, and equipment development activities preceding to the deployment of UC-4. The report is divided in two parts. Chapter 2 provides an overview of the DC microgrid architecture, main characteristics of its different components and other relevant data and background information that serve as foundation for the simulation studies. Chapter 3 summarizes results and conclusions based on data-driven simulations focused on testing different energy management and

control approaches and functions on the system- and on the battery cell level. Specifically, the following studies have been covered in this document:

- Design and development of heuristic energy management strategies for the energy management system (EMS), evaluation of their effectiveness and influence on the DC microgrid performance in different operation scenarios (Section 3.1.2).
- Evaluation of the performance of the DC microgrid with a PV system in ultra-fast EV charging in terms of reduction of power exchange with the grid (Section 3.1.3).
- In-depth modelling of the battery energy storage system (BESS) on cell level (Section 3.2.2).
- Simulation of maximum power point tracking (MPPT) control performed by the BESS string's Battery Management System (BMS) (Section 3.2.3).
- Simulation of the EV charging control by adapting the battery cell configuration and evaluation of the ability of the battery to meet the charging request with a required accuracy (Section 3.2.4).
- Simulation of the BESS recharging through the grid-connected inverter. More specifically, evaluation of the ability of the BMS control to maintain balanced cell states (Section 3.2.5).

Finally, Chapter 4 concludes this deliverable and summarizes the key findings of the studies.

2 DC MICROGRID

2.1 Energy system architecture

A single-line diagram of the complete DC microgrid is depicted at the upper half of Figure 2. It is comprised by a 312 kWh BESS, a 61 kW section of the existing PV system, two parallel-coupled three-phase 33 kW bi-directional inverters (though limited to 43 kW in total), allowing to connect the system to the low-voltage grid, and two ultra-fast high-power EV chargers with a total operational limit of 350 kW. The microgrid has a connection to the 0.4 kV AC grid. The BESS is the central element of the DC microgrid and consists of three independent battery strings of 104 kWh each, which are in turn composed of two substrings each. All the equipment, except for the PV system, is coming in a transportable standard 10 feet shipment container [9], [10]. Each component of the DC microgrid is described in detail in the following subsections.

The DC microgrid will be tested in two demo locations in the city of Rønne on the Bornholm island to explore benefits of the mobility of the solution, as well as its performance while providing different services in different operation conditions. The container will be moved between a public school Campus Bornholm and the Green Solution House (GSH) hotel every six months starting from June 2021.

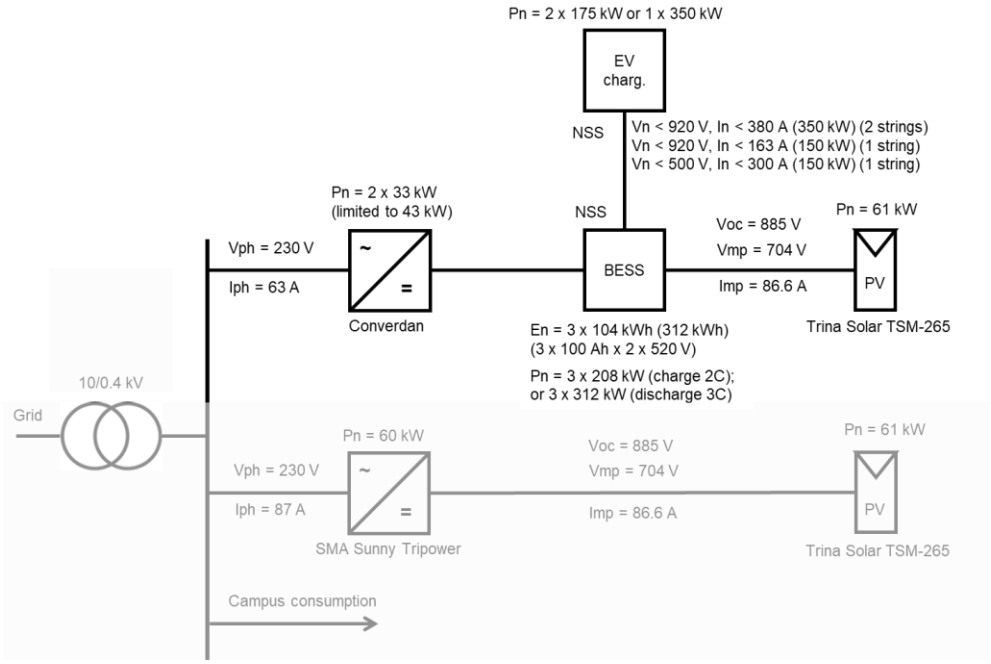

Figure 2: Single-line diagram of the DC microgrid (top half) at the main demo location, Campus Bornholm. The shaded part represents the surrounding infrastructure the system is integrated in.

The sizing parameters and composition of the DC microgrid in two locations differ by the lack of the PV system at the hotel. The following description of the system architecture refers to Campus Bornholm. However, it has general validity also for GSH with the exception that at the latter no PV system is connected to the microgrid. It is worth mentioning that all simulation studies presented in this deliverable were done considering the location of Campus Bornholm.

2.2 Control system architecture

One of the features of the battery system is that each substring in the battery system can be independently controlled. Each two substrings could be connected either in series or in parallel to achieve the necessary charge capacity and voltage level requirement of the connected components (EV, PV or inverter). The storage internal connections are structured as a matrix busbar in which different units (PV, EVs, and inverter) can be connected to any of the battery strings as needed.

Figure 3 depicts the control system architecture of the DC microgrid. The control system has a hierarchical topology. The main control unit responsible for the energy management and stable operation of the microgrid is the EMS (green block). The EMS handles the connection between the battery strings and the other components in the DC microgrid. The following minimum set of control handles for the EMS is foreseen:

- Activation/deactivation of a powerline (one of the red horizontal lines in Figure 3) for the high-power charging using a battery string in series or parallel at a specific power level;
- Activation/deactivation of a powerline for the MPPT of the PV system using a battery string;
- Charging/discharging of a battery string at a specific power level from- and to the grid.

The exact list of handles will be agreed later based on objectives of the experiments without compromising the safety of the system.

Each crossover module (COM) (orange blocks) performs the activation of serial or parallel connection of each battery string under the control of the EMS. Each String Control Module (SCM) in turn control electronic switches (MOSFETs) of each battery cell. The BESS control and cell switching logics are extensively described in [13], [14] and touched upon specific peculiarities in Sections 2.3.1 and 3.2.2.

PV MPPT and EV charging control are performed by the In-line Current Regulation and Maximum Power Point Tracking control units (ILCR/MPPT) of each battery string.

General control of the system in the container, e.g. heating and cooling, fire safety, etc. is performed by a Control of Plant unit. The control of the DC microgrid operation can be done remotely. The communication with the system is done via the 4G modem.

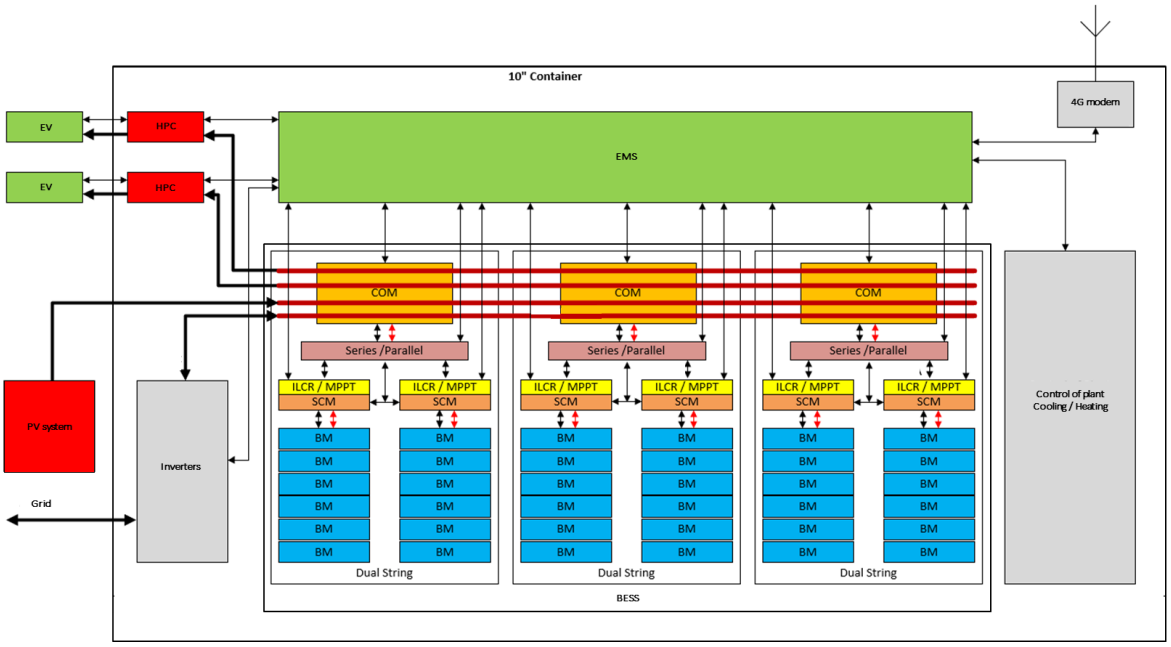

Figure 3: Block diagram of the energy and control system architecture of the DC microgrid at the main demo location, Campus Bornholm [10].

2.3 Characteristics of the system components

2.3.1 Battery energy storage system

The BESS is an innovative reconfigurable power electronic-controlled battery, manufactured by Nerve Smart Systems (NSS) [7]. It is based on a new technology, called Nerve Switch, which allows for engaging and bypassing of individual cells and thereby changing the cell topology in real-time to achieve different voltage levels. By this, DC/DC converters can be eliminated from the DC microgrid. The battery system peculiarities are described in detail in [13]-[14].

As mentioned earlier, the BESS consists of three battery strings or 6 substrings. Substrings within each string can be connected in series or in parallel. Each substring is comprised by 6 modules. Each module contains 27 cells of 100 Ah nominal capacity. The battery cells are based on the lithium-iron phosphate (LFP) chemistry.

Technical specifications for the cell, module, substring and the complete BESS is provided in

Table 1. The maximum rated voltage that can be achieved for one string is 1036.8 V and 518.4 V if substrings are coupled in series and parallel, respectively. The energy capacity and rated power per a string are 103.68 kWh and 207.36 kW, respectively.

Table 1: BESS specifications.

Battery unit	Quantity	Value	Unit
Battery cell	Technology	Lithium-ion - LiFePO4	
	Capacity	100	Ah
	Current	200	A
	Voltage	3.2	V
	Energy	0.32	kWh
	Power	0.64	kW
Battery module	Cells per module	27 in series	
	Capacity	100	Ah
	Current	200	A
	Voltage	86.4	V
	Energy	8.64	kWh
	Power	17.28	kW
Battery substring	Modules per string	6 in series	
	Capacity	100	Ah
	Current	200	A
	Voltage	518.4	V
	Energy	51.84	kWh
	Power	103.68	kW
Complete system if substrings are connected in parallel	Number of strings	6 (2x3 parallel)	
	Capacity	600	Ah
	Current	1200	A
	Voltage	518.4	V
	Energy	312	kWh
	Power	624	kW
Complete system if substrings are connected in parallel	Strings	6 (2 series, 3 parallel)	
	Capacity	300	Ah
	Current	600	A
	Voltage	1036.8	V
	Energy	312	kWh
	Power	624	kW
System information	Cooling power	< 15	kW_{th}
	Self-discharge	< 2.5	%/month
	Charge cycles	min. 6000 cycles @ DoD < 80%	
	Battery management	Nerve Switch®	
	Operating temperature	0 to +50 (charge) / -20 to +60 (discharge)	°C
	Storage temperature	from -10 to +50	°C
	Storage humidity	25 – 85	%rH

2.3.2 PV system

The location "Campus Bornholm" already has a PV system installed, with PV modules of type TSM-265-DC05A.05 from Trina Solar [15]. The PV system consists of three strings that are connected to the campus grid via one SMA Sunny Tripower 60 kW solar inverter [16] for each string. For the demonstration, one of the strings will be disconnected from its inverter and linked to the DC microgrid, while the other two strings remain in their current connection to the campus grid. The part of the PV system that will be connected to the DC microgrid has a nominal power of 61 kW. For the PV system, historical production data are available. Those data were used to estimate the expected PV production for different months of the year. Furthermore, they allowed us to test the developed control methods for the battery system in a simulative environment. Figure 4 shows the daily production curve for one PV string from June to December — the months when the battery will be installed on the campus.

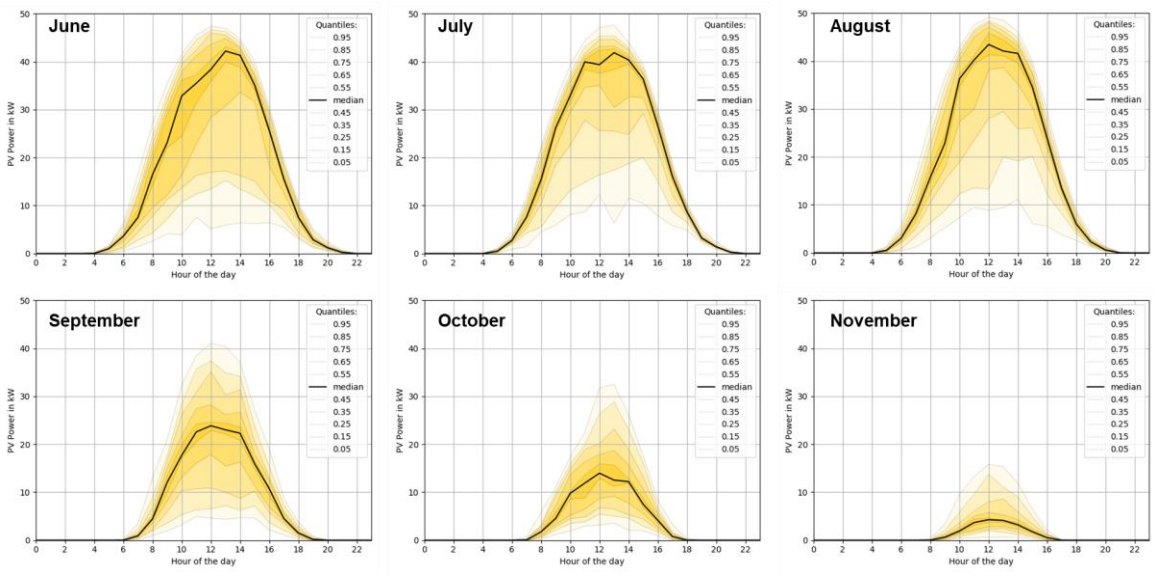

Figure 4: Historical PV production at Campus Bornholm for the months June to November (2018 – 2020). Color density indicates the quantiles of power production at the respective daytimes.

Table 2: Daily energy production (median and mean) by the PV system on Campus Bornholm from June to November (2018 – 2020).

	June	July	August	September	October	November
Median	320 kWh	333 kWh	275 kWh	164 kWh	83 kWh	20 kWh
Mean	276 kWh	297 kWh	244 kWh	155 kWh	87 kWh	28 kWh

The presented data are based on historical measurements from July 2018 to June 2020 and show the quantiles of hourly PV power. The thick line in each plot indicates the median power value,

which means that 50% of the PV power was above and 50% below this value at the respective hour. The data suggest similar PV production profiles in the months June, July, and August with a median power of around 42 kW at noon time. The median daily peak power during September, October, and November are significantly lower with 24 kW, 14 kW, and 4 kW, respectively. Also, the width of the bell curve is considerably larger in summer compared to the winter months. In June, the PV power starts ramping up from 4 a.m. and is available until 9 p.m., leading to 15 hours of power production. In November, PV power can only be expected between 8 a.m. and 5 p.m., hence 9 hours. Besides the power progression throughout the day, it is further relevant to assess the expected daily energy production in the different months. Figure 4 compares the median and mean daily energy from June to November for the same period as for the power profiles. The values underline the significant difference in energy production for the different months. While in June and July more than 50% of the days had PV energy of more than 320 kWh, the median daily energy decreases down to 20 kWh in November. This emphasizes that the energy management for the microgrid has to be able to operate with a wide range of PV production. In summer, the daily energy production of the PV often exceeds the total energy capacity of the BESS. This makes it necessary to export energy to the grid on time, as PV energy cannot be extracted if all strings are fully charged. In contrast, the PV production in winter is not enough to fully charge one single EV. Consequently, it is required to import enough energy from the grid to fulfil the EV charging needs. More on this topic will be addressed in Section 3.1.

2.3.3 EV charging

The two ultra-fast EV chargers integrated into the DC microgrid are developed by NSS. The chargers are compliant with the Combined Charging System (CCS) 2.0 standard. The charging station provides a possibility to charge 2 electric vehicles in parallel with a maximum power output of 175 kW or one EV with up to 350 kW.

For the modelling and simulation studies involving EV charging it was essential to define a range of expected EV battery capacities and charging power requested, as well as to better understand the EV charging pattern over the day. For the former, statistical data for the existing EV fleet on Bornholm for May 2020 provided by [17] were analysed. The data contain information on brand, model, and number of EVs and hybrid EVs registered on Bornholm. Based on the data, 11 EV models with a total number of 31 EVs compliant with the CCS charging standard, which is used in the system, were identified. The resulting list of EVs with some specific characteristics can be found in Table 3.

Table 3: EVs on Bornholm compliant with the CCS charging standard. Data are from [17] for May 2020.

Brand	Model	Variant	No	Energy capacity, kWh	Max. charging power, kW
Audi Quattro	e-tron	50	1	64.7	120
Audi Quattro	e-tron	55	1	83.6	155
BMW	I3	120 Ah	5	37.9	49
Jaguar	I-Pace	EV400	1	84.7	104
Kia	e-Niro	39 kWh	2	39.2	50
Renault	Zoe	ZE40 R110	3	41	45
Tesla	Model 3	LR dual motor	5	70	190
Tesla	Model 3	LR performance	3	76	250
Tesla	Model 3	SR plus	4	50	160
Volkswagen	Golf	e-Golf	4	32	40
Volkswagen	Up!	e-Up!	2	16	40

Based on the data, the average usable energy capacity was estimated as 50.4 kWh, and the average maximum DC charging power request as 111 kW. The expected number of plug-ins per day for Campus Bornholm was estimated based on real-life measurements from a DC charger placed at the parking lot in front of building 325 of DTU Lyngby campus [19] due to unavailability of data for the Bornholm's demo locations. The data were taken for a period from June to December 2018. The estimation resulted in defining minimum daily number of plug-ins of 1 and maximum of 6. The numbers were adapted, since there are 2 chargers in the system.
Based on [18], the average plug-in SOC for fast EV charging was estimated as 40-50%, while the minimum – 20%. The latter value was used for defining worst case scenarios in the simulation studies. The average plug-out SOC was estimated at the level of 80%.

2.3.4 Inverter

The DC microgrid is connected to the AC grid through two parallel-connected three-phase bidirectional inverters of type AFE333KAC from Converdan [20] with a combined rated active power of 66 kW. For simplification purposes, we will use the term inverter in singular in the rest of the document, but always refer to the parallel connection of the two inverters. The grid connection at Campus Bornholm is limited to 63 A per phase. Thus, the maximum active power that can be exchanged with the grid for the three-phase connection is 43.57 kW. The inverter ideally operates in a DC voltage range of 800-900 V. The conversion between AC and DC is not loss-free. Therefore, for the simulations the inverter is modelled with an efficiency characteristic in dependency of the active power. Since the datasheet does not provide any efficiency characteristic and measurements were not available, a generic inverter characteristic was considered as shown in Figure 5.

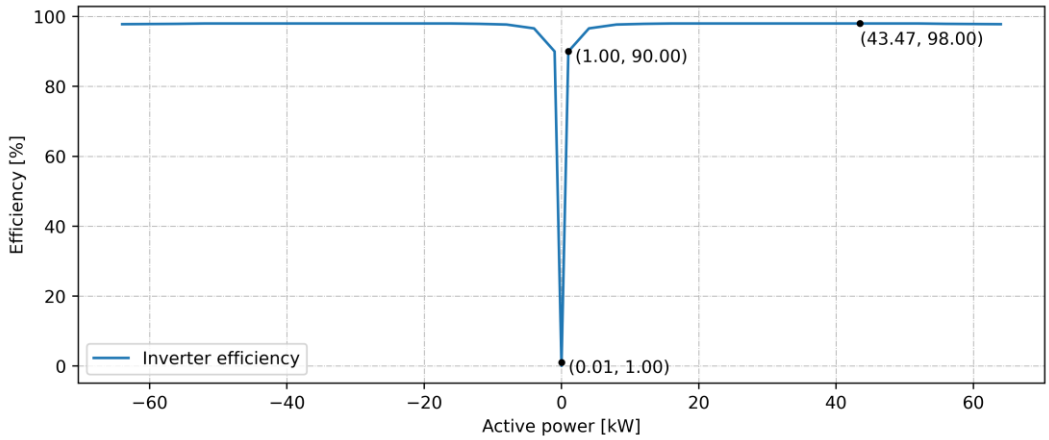

Figure 5: Inverter efficiency characteristic in dependency on the power.

The inverter efficiency is defined for positive (exporting energy into grid) and negative (importing energy from grid) since it has bi-directional capabilities. The efficiency is symmetrical around 0 kW, so the direction of power flow is irrelevant for the efficiency of the inverter. However, the efficiency is highly affected by the amount of power that flows through it. It reaches efficiencies of around 98% at maximum power (43.47 kW due to limitation of 63 A grid connection). When operating the inverter at low power (1 kW), the efficiency drops to around 90%. It is assumed to be 1% at power level of 0.01 kW.

2.4 Campus Bornholm consumption

This section gives insights on the consumption profile of Campus Bornholm. Figure 6 shows the system layout of the campus before and after the installation of the DC microgrid. Historical measurements are available for the PV production, and for the imported and exported energy at the grid connection point. Based on this information, the consumption of the school is calculated as

$$P_{cons} = P_{PV} + P_{import} - P_{export}$$

An analysis of the data allowed us to calculate the historical self-consumption of the school, i.e. the percentage of consumed energy that was provided by the own PV system. Additionally, the historical data were used to estimate daily consumption profiles of the school. The obtained profiles serve as an input of models investigating energy management strategies for the new storage system. The most important findings are summarized in the following.

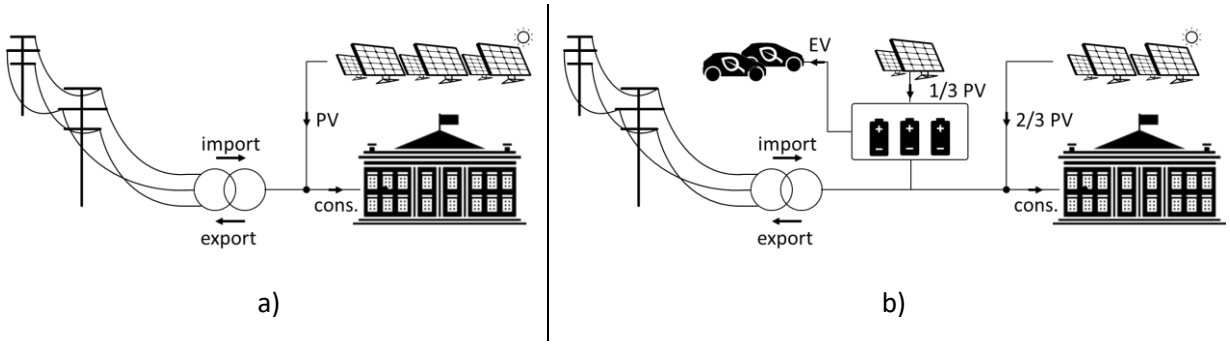

Figure 6: System layout a) before and b) after installation of DC microgrid

Table 4 summarizes the historical data for June – November (2018 and 2019). Based on consumption, imported and exported energy, as well as PV production, the level of self-consumption is calculated for the different months with

$$\text{self-consumption} = \frac{E_{PV} - E_{export}}{E_{cons}} = \frac{E_{PV} - E_{export}}{E_{PV} + E_{import} - E_{export}}$$

In the table, the historical self-consumption is given in the column "w/o DC microgrid", referring to the system layout before installation of the DC microgrid (Figure 6 a). The self-consumption ranged between up to 65% in the summer months and 4% in November. This large difference is mainly caused by two factors. First, the PV production is significantly higher in the summer months, as previously shown in Section 2.3.2. Second, the consumption of the school increases in the winter months: Considering 2019, the overall consumption in June was 29882 kWh, while in November

47442 kWh, thus 60% larger. With the installation of the DC microgrid, the overall level of self-consumption is expected to change, since 1/3 of the PV system will be connected to the DC microgrid, as illustrated in Figure 6 b. However, the influence on the level of self-consumption highly depends on how frequently the EV fast-chargers will be used. To quantify the impact of the installation, the historic data were used to calculate both the worst and best case, assuming the microgrid was already installed in 2018. The worst case for the level of self-consumption of the Campus buildings is, if all the PV energy flowing into the microgrid is used for EV charging. The corresponding values are given in the column "With DC microgrid/worst case". As seen in the table, this causes the campus self-consumption to decrease to 2/3 in each month. In contrast, if no EVs are using the chargers, the BESS can be utilized to increase the self-consumption compared to the initial setup. Storing excess energy during hours with high PV production (avoiding grid export) and using it in hours with low PV production (avoid grid import) reduces the energy exchange with the grid and, consequently, increases the degree of self-consumption, as shown in previous studies [11] [12]. The corresponding values are given in the column "With DC microgrid/Best case". The assessment suggests, that the BESS can help to overall increase the level of self-consumption during all months. Especially in July, where the overall consumption is relatively low, the self-consumption could be increased up to 96%. Taking all this into account, the level self-consumption after the installation is expected to lie between the best and worst case presented in Table 4.

Table 4: Overview of historical monthly consumption, imported and exported energy, and PV production. Information is given for the months June to November, where the battery will be installed at the campus.

Year	Month	Consumption (kWh)	Import (kWh)	Export (kWh)	PV (kWh)	Self-consumption		
						w/o DC microgrid	With DC migrogrid	
							Worst case	Best case
2018	June	28,279	10,536	11,903	29,646	63%	42%	78%
	July	16,192	6,078	17,157	27,271	62%	42%	88%
	August	27,605	14,939	8,405	21,071	46%	31%	61%
	September	30,545	18,113	4,122	16,554	41%	27%	48%
	October	36,759	28,710	1,316	9,365	22%	15%	25%
	November	38,274	35,434	303	3,143	7%	5%	8%
2019	June	29,882	15,295	7,645	22,232	49%	33%	63%
	July	12,569	4,447	19,770	27,892	65%	43%	96%
	August	36,167	18,371	6,435	24,231	49%	33%	60%
	September	41,826	30,571	38	11,293	27%	18%	28%
	October	44,696	38,191	359	6,864	15%	10%	16%
	November	47,442	45,481	24	1,985	4%	3%	4%

Besides the total monthly energy values, it is relevant to look at the daily consumption profile of the campus. Table 5 shows the daily profiles of consumption and grid import for different months, based on measurements from 2018 to 2020. The shape of the consumption profile is similar to the PV profile presented in Section 2.3.2, and shows a gaussian-like progression with peak around noon time. However, the consumption shows a clear base load, i.e. the consumption does not drop to zero at night but rather keeps a constant level. When comparing the consumption profiles of the different months, it can be seen that the consumption increases towards the winter months – both the peak and the base load. This is in line with the total consumption values reported in Table 4. Furthermore, it is apparent how the summer holidays reduce the consumption in July. When comparing the imported power to the consumption, it can be seen how in summer the import is significantly smaller than the consumption. This is due to the higher production of the PV system, which reduces the need to import power from the grid to cover the demand. During the winter months, the profiles of consumption and import are nearly identical, only around noon time the PV production reduces the need for grid import.

Table 5: Daily profiles of consumption and grid import for different months. The graphs give the hourly quantiles between 5% and 95% quantile in 5% steps, as well as the median power as the thick line. The profiles are based on measurements between 20.06.2018 and 19.06.2020.

Month	Consumption	Import
June	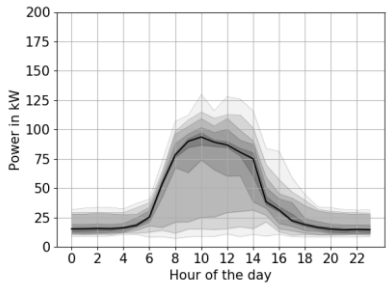	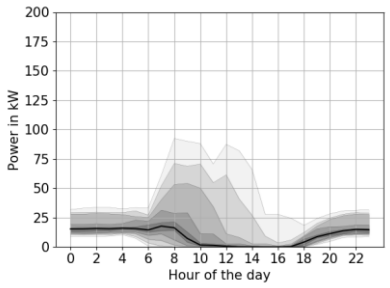
July	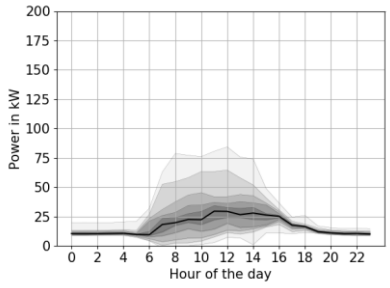	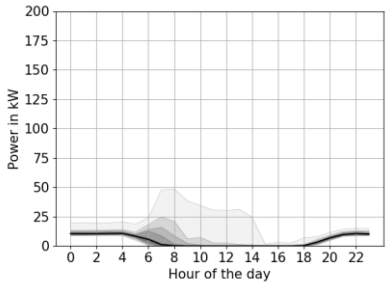

August	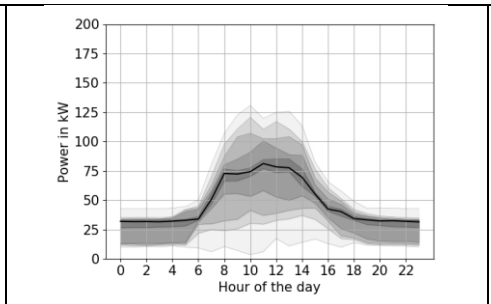	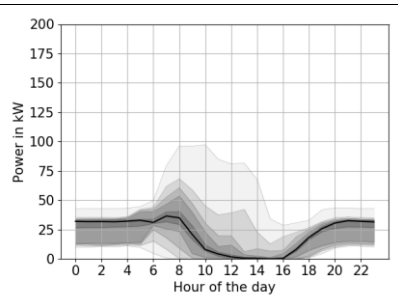
September	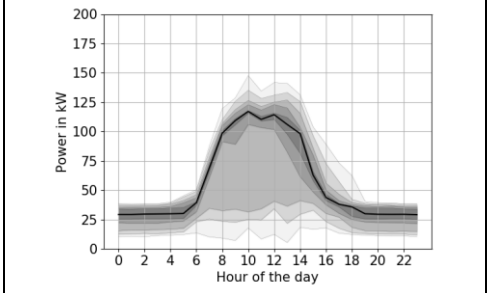	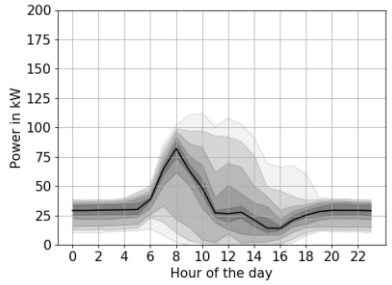
October	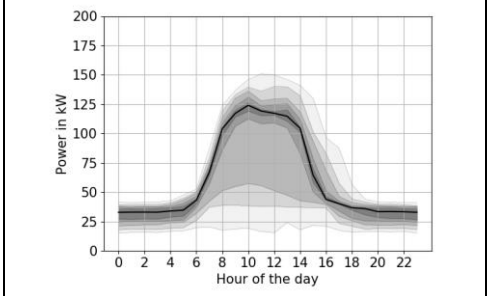	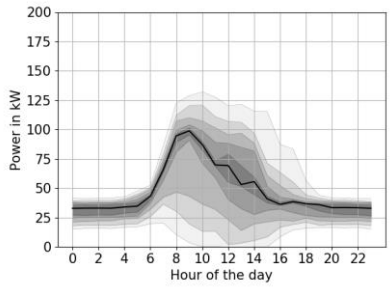
November	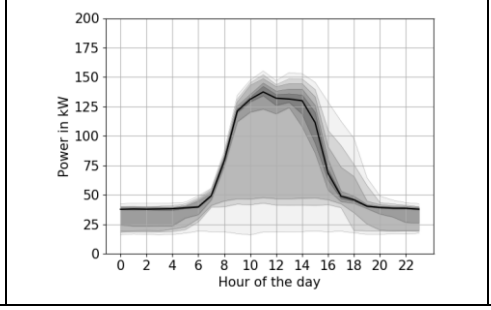	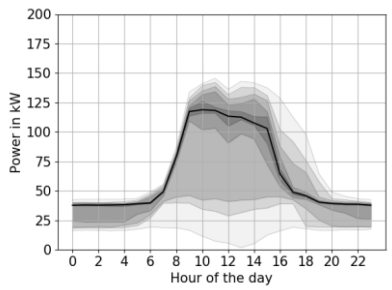

Another characteristic worth considering is the difference in the consumption profiles on working days and weekends. Table 6 shows this comparison for two exemplary months (June and November). As seen from the graphs, the profile is different on weekends, where the consumption only consists of the baseload of the school building. The baseload is generally higher in November as the median power value is approximately three times higher than in June. The difference between working days and weekends is an important detail that can be considered in the energy management of the BESS. By using this knowledge, the DC microgrid with its battery storage can

potentially be used to provide peak shaving functionality for the whole campus grid, thus increasing self-consumption and decreasing electricity costs.

Table 6: Comparison of daily consumption profiles on working days and weekends.

Month	Consumption Working Day	Consumption Weekend
June	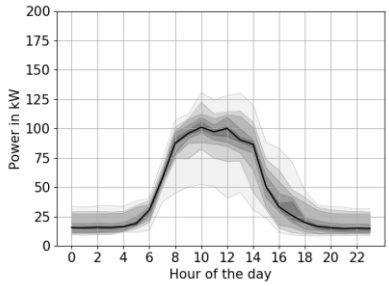	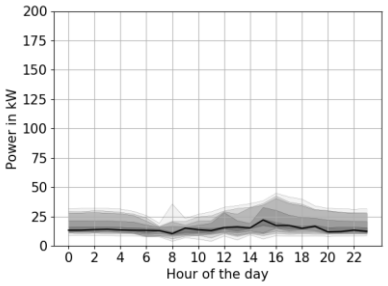
November	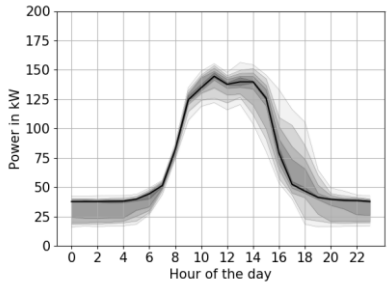	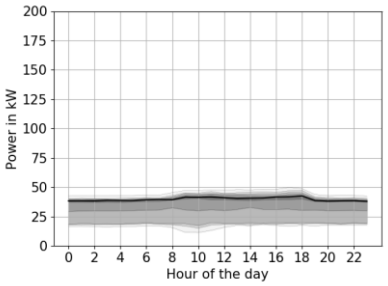

3 MODELLING AND SIMULATION RESULTS

The design of the battery system allows controllability on two different levels. On a high level, the three strings can be switched between the different units (PV, EV, inverter) via the busbar matrix. The responsible control unit on this level is the Energy Management System (EMS), as the decision making is primarily based on the energy level of each string. On a low level, the reconfigurable cell design allows to change the number of active cells in each string in a real-time fashion. This ability to actively control the string voltage enables the strings to be directly coupled with the other components, without the need for power converters. The responsible control unit on this level is the Battery Management System (BMS).

The modelling activities were organized in the following manner. Simulations on system level were focused on the power flow between the different components of the DC microgrid, with the EMS being the central control unit of the investigation. A summary of the models and simulation results is given in Section 3.1. The performance of the reconfigurable design was assessed with in-depth technical models on cell level, with the BMS being responsible for the decision making. The main findings of this focus can be found in Section 3.2.

3.1 Energy management system

3.1.1 Control objectives

Figure 7 provides a high-level overview of the system indicating the power flow to and from the battery system. While the PV system is supplying power to the battery, the EVs are consuming power. The inverter allows a bi-directional power exchange with the grid. Since the energy stored inside the battery strings is subject to the power supplied and consumed by the connected components, the battery must keep its state-of-charge (SOC) within acceptable limits in order to guarantee a reliable and uninterrupted operation of the overall system.

The device responsible for monitoring, planning, and controlling the SOC of the battery is the EMS, which has to make sure that the objectives for operating the individual components (PV, EVs, inverter) are being fulfilled at any point in time. To achieve this, the EMS is deciding which battery string is connected to which component. Furthermore, it continuously adjusts the power setpoint for the inverter, thus managing the energy exchange with the grid.

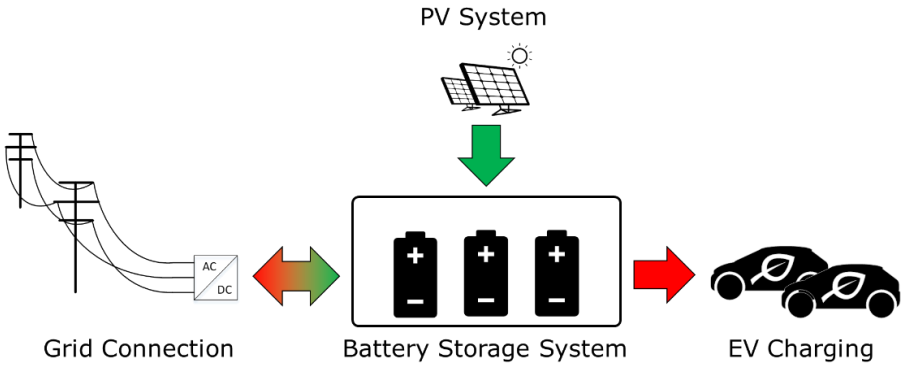

Figure 7: Overview of the DC microgrid and the power exchange with the connected components at Campus Bornholm. Green arrow indicates power flow to battery; red arrows indicate power flow from battery.

In order to determine the optimal SOC of the battery strings, the objectives for operating the different components have to be included in the decision-making.

The objective for operating the PV system is to maximize the generated energy. To achieve this, the EMS must ensure that during hours of available solar energy, the PV system is always connected to a battery string with chargeable capacity. When all strings are fully charged, the battery cannot receive any more energy from the PV system, therefore the produced power is lost.

The objective for the EV charging is to fulfil the vehicles' charging needs. Therefore, the EMS must ensure that the string which is assigned to the EV connector has a sufficient SOC. In case the battery is fully depleted, no charging power can be provided to the EVs.

With regard to the grid connection, the objective could differ. When providing ancillary grid services (e.g. primary frequency control) or when trading energy on the electricity market, the objective is to maximize revenues. Therefore, the task of the EMS is to ensure that the scheduled services can be delivered. Furthermore, the inverter can be operated to balance the power exchange between Campus Bornholm and the grid. In this case, the goal is to minimize the overall electricity costs of the campus ("behind-the-meter" approach). There could be also specific objectives to minimize the power import to the grid, by this increasing self-consumption of the DC microgrid, or energy export from the grid to demonstrate self-sufficiency of the system in providing high-power EV charging when connected to the weak grid.

However, simultaneous fulfilment of EMS objectives and power and energy needs and objectives of different system components can be challenging since different components may have contradicting expectations for the SOC of the battery strings. For example, to be able to store as much PV production as possible, the SOC of the battery string needs to be low. At the same time, to be able to fully charge an EV or a series of EVs, the SOC of the string it is connected to needs to

be high enough. For the grid connection, the ideal battery SOC strongly depends on the scheduled service as well as the current power flow direction.

3.1.2 Heuristic control

A dedicated study aiming at the design of energy management strategies and evaluation of their effectiveness and influence on the DC microgrid system performance was carried out. It was specifically aimed at understanding,

- to what degree the EMS objectives and component functionalities are satisfied when applying different SOC targets to the battery strings,
- which operational scenarios challenge the system the most,
- what is the “limit” of the system in terms of the number of subsequent EV charging,
- what is the efficiency of the system and its separated components in different operation modes and following different EMS strategies.

The work is reported in detail in [21]. A mathematical model of the DC microgrid, comprised of three BESS strings, two EV fast chargers, a PV system, and two grid inverters, sized as described in Section 2, was implemented in the MATLAB & Simulink environment. The model was built on the power and energy level. The focus was given to the modelling of the EMS and the development of energy management strategies, while the other components were modelled is a simplified way yet sufficient for the purposes of the study. Herewith, each of the three battery strings were modelled based on the Coulomb counting approach (but integrating the power instead of current to get energy as output) and taking into account internal power losses. Figure 8 depicts the efficiency characteristics of a battery string based on the BESS model described in Section 3.2.2 [13], used in the study. When connecting the battery string to the inverter, the efficiency is expected to be greater than 96% since the inverter power is limited to 43.47 kW, while for the case of fast EV charging at 150 kW the efficiency is significantly lower, resulting at 87.27%. The SOC range allowed for the operation of the battery is from 10% to 90%.

The PV system was modelled as an hourly power production profile based on the data described in Section 2.3.2, while the EV charging – based on the findings reported in Section 2.3.3 (more details are provided further in this section). The inverter was modelled with an efficiency characteristic as a function of the active power, depicted in Figure 8.

A thermal model of the system was also built for the analysis of the temperature dynamics in 5 different zones of the container, as well as auxiliary power consumption of the thermal management units in the system. The temperatures are modelled based on heat balance equations, while the auxiliary power consumption - based on the control logics and ratings of different components.

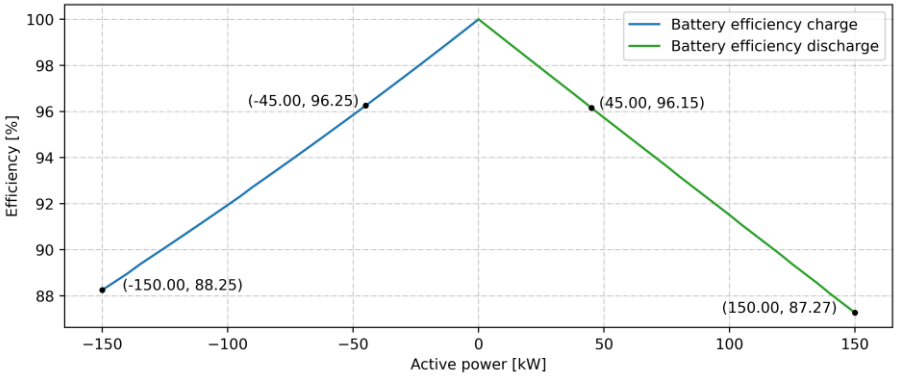

Figure 8: Efficiency characteristics of the battery string as a function of the active power.

The EMS is modelled taking into account objectives and constraints described in Section 3.1.1. The controlling algorithm had to ensure that only one component is allowed to be connected to a battery string at a time, and an EV-connected battery string cannot be changed during charging.

Three energy management strategies differing by the SOC target for the strings, were designed:

- **Strategy 1** assigns an SOC target of 50% to a battery string. This way the battery strings are always in state where they can either be connected to an EV or the PV since they are not too empty or too full.
- **Strategy 2** implements a dead band with a lower and upper SOC limit of 50% and 70% respectively instead. This way the harvested PV energy is not exported into the grid before the SOC level reaches 70% to be able to use it directly when there is an EV charging demand.
- **Strategy 3** is based on strategy 2, but utilizes the ideal one-hour ahead PV forecast to dynamically adjust the lower SOC dead band limit between 30% and 50%, while keeping the upper limit at 70%. This way, harvested PV energy is prioritized to recharge the batteries rather than using the inverter, thus reducing the energy import to the grid.

To analyse the performance of the model, 9 operation scenarios formed by different combinations of PV production and EV charging load over a week were created. Designations of the different scenarios are listed in Table 7.

Table 7: Scenarios formed by different combinations of PV production and EV charging frequency (the first letter refers to the PV and the second – to the EV).

	Low EV	Medium EV	High EV
Low PV	*ll*	*lm*	*lh*
Medium PV	*ml*	*mm*	*mh*
High PV	*hl*	*hm*	*hh*

Low, medium and high PV production scenarios were created based on the real PV production data from the one third of the Campus Bornholm's PV system, as described in Section 2.3.2. Specifically, 1 week in November 2018, 1 week in September 2018 and 1 week in June 2018 were chosen with a total energy production of 145.3, 1484.9 and 2278.7 kWh, respectively.

Low, medium and high EV charging load scenarios are created based on data on the number of plug-ins per day, required energy per charge and the average DC charging power defined in Section 2.3.3. The plug-in and plug-out SOCs used are 20% and 80%, respectively. The required energy per charge and DC charging power are kept constant at 30.24 kWh and 110.9 kW respectively, while the number of plug-ins per day is 1 (low), 3 (medium) and 5 (high) per each charger (2, 6, and 10 chargings in total over a day, respectively). A time shift of one hour is implemented between charging requests to each charger. Figure 9(a) provides an example of the PV production and EV charging profiles in *hh* scenario for one day. It shows also how differently the switching and the SOC dynamics of battery strings evolve when the system is forced to follow each of three strategies.

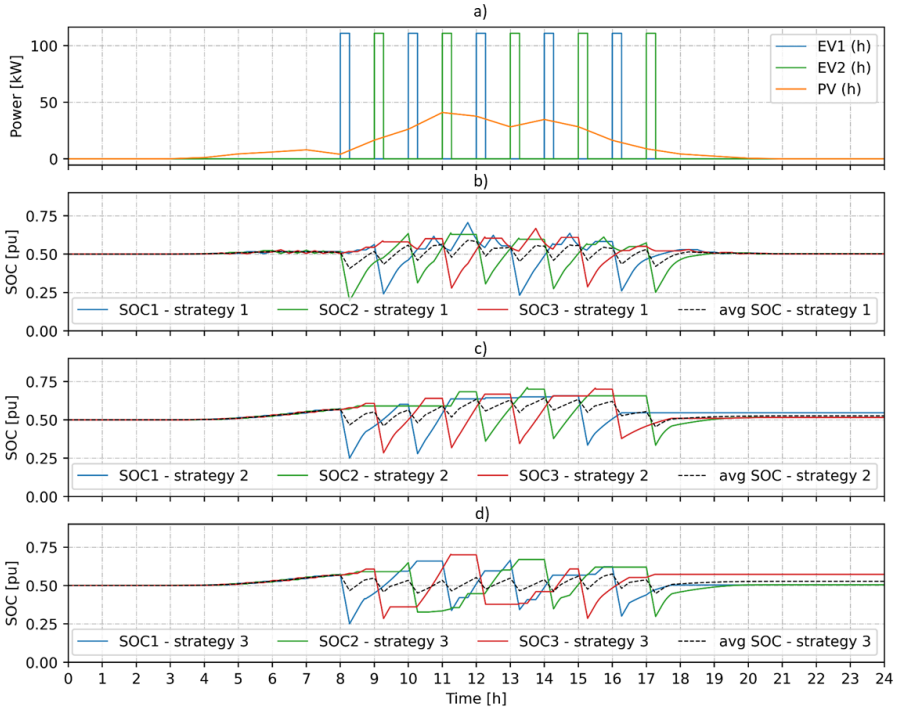

Figure 9: Visualisation of a) high PV production and high EV load profiles (*hh* scenario), b), c), d) - switching and SOC dynamics of battery strings (SOC1, SOC2, SOC3) when the system follows Strategies 1 (b), 2 (c) and 3 (d) over a day.

Figure 10, Figure 11 and Figure 12 showcase an example of the thermal management of the container as well as the auxiliary power consumption of the thermal management, control and monitoring components when the system follows Strategy 1 in the *hh* scenario (a summer day).

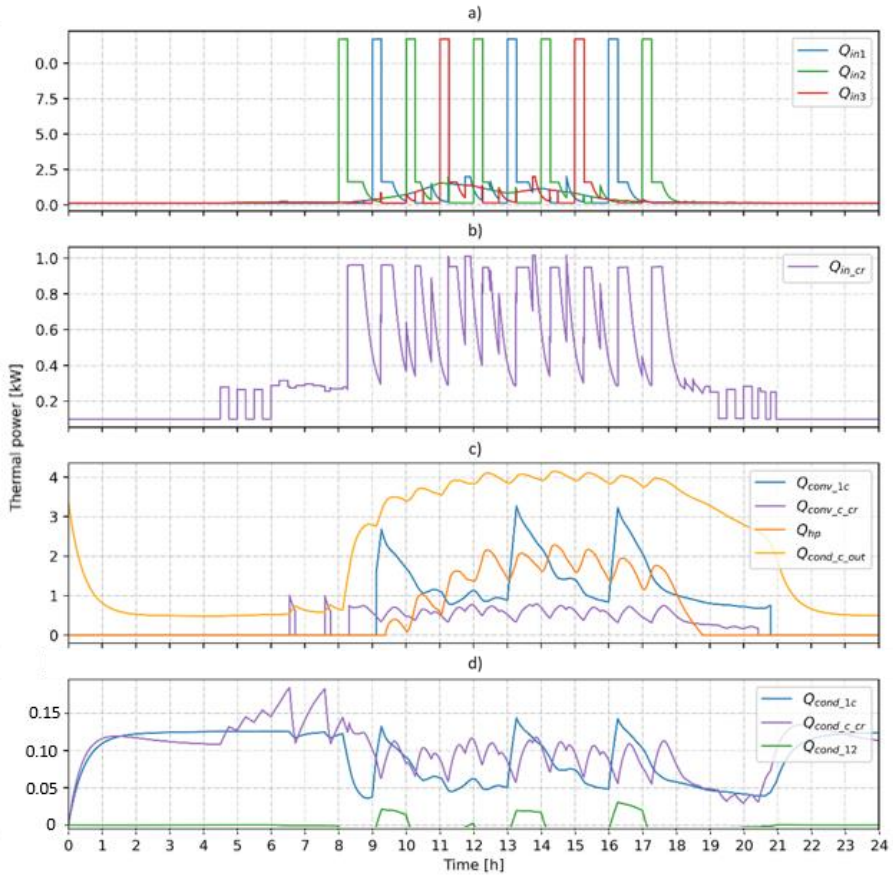

Figure 10: Heat flows in the container while operating the system with Strategy 1 and *hh* scenario (Figure 9(a) and (b)) over a day: a) generated by each battery string, b) generated in the control rack, c) Q_{conv_1c} - between string 1 and the container, Q_{hp} – removed by the heat pump, $Q_{conv\_c\_cr}$ - between the control rack and the container, $Q_{cond\_c\_out}$ - dissipated through the container walls to the outside. d) Q_{cond_1c} - between string 1 and the container, Q_{cond_12} - between strings 1 and 2, $Q_{cond\_c\_cr}$ - between the control rack and the container.

The initial temperature (at time = 0 h) in all five zones in the container is 25°C. After several hours of the simulation the temperature in the middle of the container Tc drops due to the heat dissipation through the container walls ($Q_{cond\_c\_out}$), since the outside temperature is lower than in the container. At time = 8 h, when the first EV starts charging by the string 2, its temperature Tin2 and the control rack's temperature T_{cr} start increasing, so does heat flows from the respective components. In parallel, strings 1 and 3 are getting charged from the PV and the grid. T_{cr} increases

much faster than Tin2. This can be explained by the lower thermal capacitance of the control rack (79.8 kJ/K vs. 1232 kJ/K). When T_{cr} reaches and goes above 30°C the convective heat flow from the control rack $Q_{conv\_c\_cr}$ increases due to fans being activated. After the first charging session is finished Tin2 slowly decreases, while Qin2 decreases to 0 kW.

Between 8 and 18 h, the battery dual strings alternate between charging EVs and being recharged from either PV system or the grid. This heats up the battery dual strings and the control rack, and the generated heat is transferred to the container through conduction and convection. As the container temperature (T_c) increases so does the heat pump output (Q_{hp}). The maximum thermal power of the heat pump is approximately 2.1 kW for a container temperature of 27.2°C at around 13.5 h.

The maximum battery dual string temperature is T_{in3} = 38.3°C at time of approx. 14 h. After all strings finished daily charging sessions, string temperatures decrease down to 25°C. This is due to the hysteresis implemented in the fan control logic, which turns them off at 25°C and on at 30°C. At the end of the day the container temperature drops to approximately 17°C since the outdoor temperature is lower and the thermal resistance of the container is relatively small (0.0032 K/W).

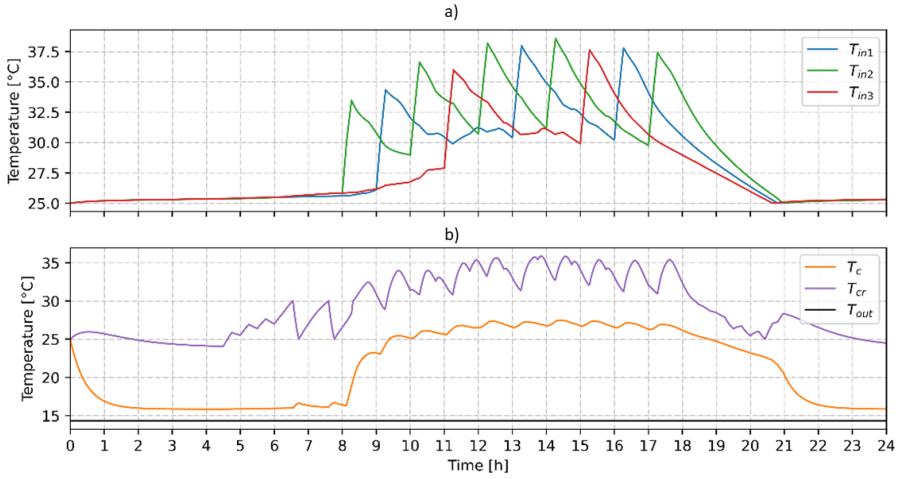

Figure 11: Temperatures in the container while operating the system with Strategy 1 and *hh* scenario (Figure 9(a) and (b)) over a day: a) in battery strings 1, 2 and 3, b) Tc – in the middle of the container, T_{cr} - in the control rack, T_{out} - outdoor temperature (T_{out} = 14.3 °C).

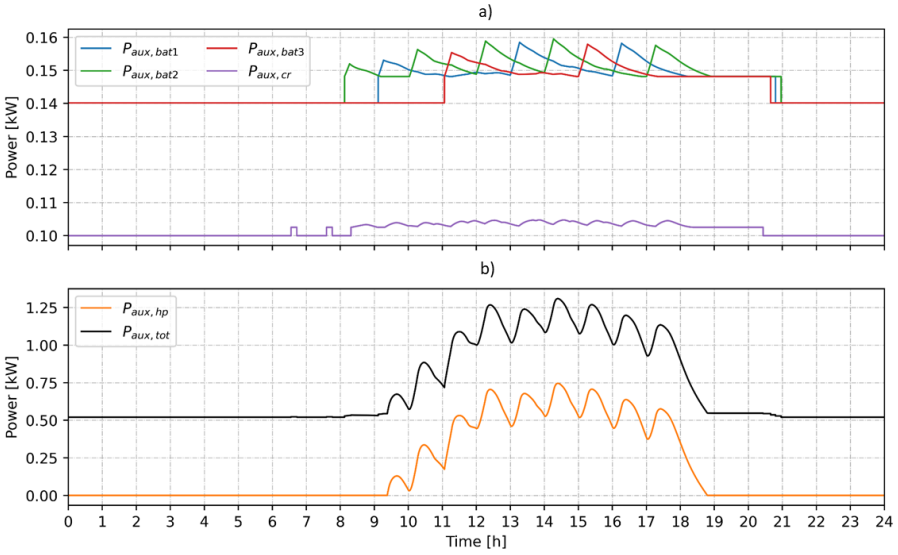

Figure 12: Auxiliary power consumption while operating the system with Strategy 1 and *hh* scenario (Figure 9(a) and (b)) over a day: a) of strings and components in control rack, b) of heat pump and the whole system.

As could be seen in Figure 12, each battery dual string has a constant auxiliary power consumption of approximately 140 W, used by the string controller and module controllers. Auxiliary power consumption of the inverter and fans in the control rack $P_{aux,cr}$ depends on the activity of the fans and therefore the temperature. The fans are activated in the moment the temperature reaches and goes above 30°C. The power consumption of fans is proportional to the cube of the normalized fan speed. For this specific study case, the fans are running at not more than 50% of speed, which results in relatively low auxiliary consumption (around 12.5% of their rated power). The heat pump auxiliary power consumption ($P_{aux,hp}$) reaches maximum 0.75 kW and takes the bigger share in the total system consumption, which is around 0.52 kW throughout the day and does not go above 1.3 kW in peak.

The performance of the system when following each of the strategies was simulated for 9 different operation scenarios over seven days. The results showed that for all investigated combinations all the requested EV energy is delivered, and all the produced PV energy is harvested, hence the EV and PV objectives are fully satisfied, while SOC levels of the strings are kept at operational limits for all strategies. However, the number of full charging cycles, and therefore influence on the battery ageing, as well as amount of the energy exchanged with the grid, auxiliary energy consumption, battery, inverter and system losses, and system and component efficiencies differ from strategy to strategy.

Since one of the benefits of the technology is a possibility to perform fast EV charging when having a weak grid connection, it was important to compare the amount of energy exchanged with the

grid. Figure 13 visualizes exported ($E_{grid,exp}$), imported ($E_{grid,imp}$) and total energy exchanged with the grid ($E_{grid,tot}$) over a simulation period of 7 days following each of the three strategies. It shows that generally Strategy 2 and 3 allow exporting less energy and reducing the amount of imported energy and therefore the total energy exchange with the grid gets lower. Herewith, the higher the PV production, the smaller grid energy exchange could be achieved. For example, for the scenario *hh* and Strategy 3 $E_{grid,tot}$ is reduced by approximately 76% compared to strategy 1.

Strategy 3 allows to import less energy compared to the remaining two strategies thanks to the dynamic lower limit of the SOC target. The other two important performance metrics are energy losses (comprised of auxiliary consumption of different components, as well as thermal losses) and the energy efficiency of the system and specific components.

There is a noticeable reduction of the system energy losses for scenarios with medium and high PV production and low, medium and high EV load for Strategies 2 and 3 compared to Strategy 1, as less energy is exchanged inside the system. For example, using Strategy 3 in scenario *hh* results in a system energy loss reduction of approximately 22% compared to Strategy 1 [21].
The system efficiency is slightly higher for the Strategy 1 compared to the Strategies 2 and 3 in all scenarios (Figure 14). Herewith, the inverter efficiency is marginally higher while the battery efficiency is generally lower for Strategies 2 and 3 compared to Strategy 1. This is due to the fact that in Strategies 2 and 3 the inverter is used less hence the losses from EV charging weight higher.

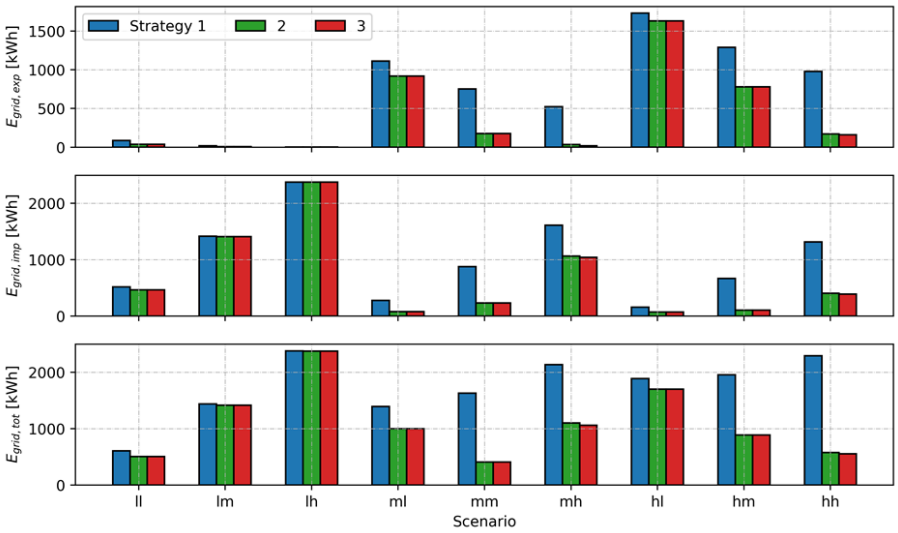

Figure 13: Visualisation of the exported ($E_{grid,exp}$), imported ($E_{grid,imp}$) and total grid energy ($E_{grid,tot}$) integrated over 7 days when system follows different strategies and scenarios.

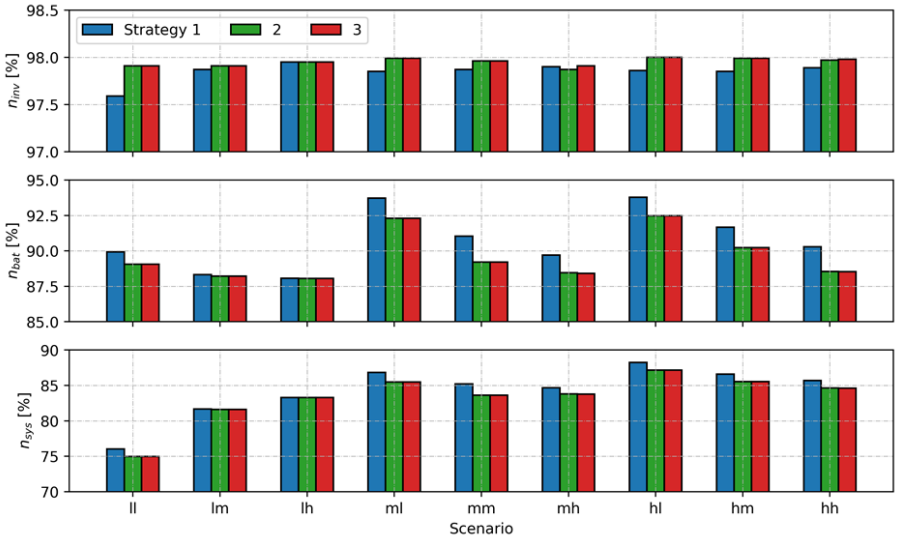

Figure 14: Visualisation of the inverter (n_{inv}), battery (n_{bat}) and system efficiencies (n_{sys}) when system follows different strategies and scenarios simulated over 7 days.

Two additional stress cases were tested to find out the maximum number of consecutive EV chargings that the system could fulfil when the PV production is almost absent. Two different strategies are tested: Strategy 3 introduced earlier and a modified Strategy 1 with an initial SOC level and SOC target of 90% instead of 50%.

A charging pattern of five subsecutive EV chargings per each charger, used in a high EV scenario, with the requested energy of 30.24 kWh and charging power of 110.9 kW was adapted by reducing the interval between chargings for 1 charger from 1 h to 1.5 min, while chargings happen in parallel in two chargers. Figure 15 illustrates the evolution of the battery strings' SOCs when operating the two strategies over four hours in the middle of the day in November.

Figure 15 shows that following Strategy 3 the BESS can afford full charging of only 3 EVs. This is due to the low initial SOC, as well as due to the fact that one string remains connected to the PV even if the production is low, therefore cannot be used for EV charging or recharging.

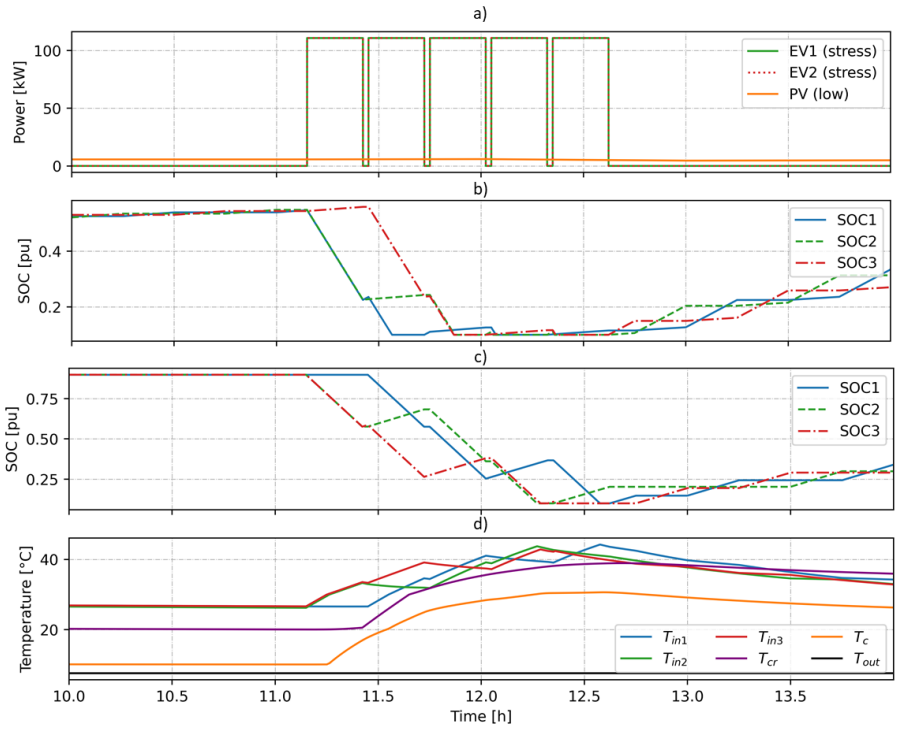

Figure 15: SOC evolution of three strings during the stress tests with the PV production close to zero and extreme EV charging events, representing a day in November: a) PV generation and EV charging profiles, b) and c) – SOC progressions when running Strategy 3 and modified Strategy 1, respectively. d) Temperature progressions in battery strings (T_{in1}-T_{in3}), control rack (T_{cr}), container (T_c) and outside the container (T_{out} = 7.6 °C) for the modified Strategy 1.

In turn, when following Strategy 1 with the initial SOC of 90% and the SOC target of 90%, the system is able to fully charge 6 EVs (although at time around 12.05 h Strings 2 and 3 get connected to the 7th and 8th EVs, they are not able to deliver the full requested energy until get disconnected due to the low SOC) (Figure 15(c)). This number is achieved because the maximum amount of energy is ready for charging EVs in the beginning of the day. Furthermore, instead of harvesting PV energy on the remaining battery string, the inverter is used to recharge the batteries faster. This way, EV charging objective is prioritized above the PV objective. Herewith, as could be seen in Figure 15(d), the maximum temperature of the battery strings in operation reaches maximum 44.2°C, which is within the safe operational range of max 50°C, according to the BESS specifications (

Table 1).

The results of the study allowed to conclude that all strategies initially proposed generally fulfil the requirements assigned to the EMS if the EV charging events are distributed with 1 hour delay. In turn, stress cases showed that if the PV production is low and very frequent EV charging is detected the strategies require some adjustments of the SOC target, prioritizing EV objectives above the PV objectives. An improvement could also be achieved by lifting the string switching constraint, allowing to switch between strings in the process of EV charging.

3.1.3 Optimal control

The DC microgrid investigated in the UC4 offers the possibility of providing ultra-fast charging with a weak grid capacity connection. A conservative solution for the installation of EV ultra-fast chargers is to buy the necessary infrastructure and a larger grid capacity connection. The infrastructure would be directly connected to the grid, resulting on large requests of power at the grid connection point.

The investigation described in this section was dedicated to a comparative analysis of the performance of the DC microgrid in terms of power exchange with the grid compared to the conservative solution while facilitating the local usage of the PV production. The complete work in described in [22].

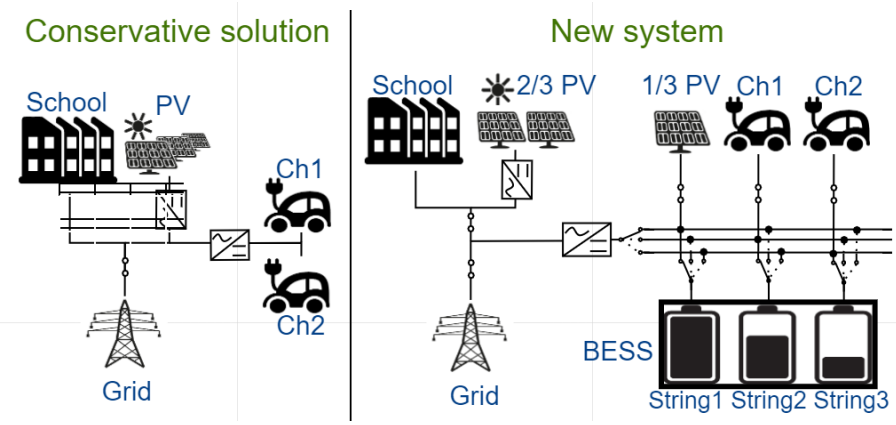

Figure 16. Comparison of the conservative solution with the new system [22].

The two configurations, conservative solution and DC microgrid are provided in Figure 16, whereas the capacities of the components are summarized in Table 8.

Table 8. Installed capacities. *Each string is considered with max. charging current 2C (208 kW) and discharging current 3C (312 kW) [22].

Component	Installed capacity
BESS strings	104kWh / (208 kW/312 kW)*
PV	180 kWp (1/3 PV→60 kWp)
Ch1/ Ch2	175 kW/175 kW
Grid inverter	66 kW

Table 9: Electricity prices per kWh.

c_t^e	c_t^i	c_t^{eSc}	c_t^{Ch}
0.22 DKK	1.9 DKK	1.9 DKK	3.7 DKK

The day-ahead unit commitment problem of the DC microgrid is here implemented as a Mixed Integer Linear Programming Problem in Matlab. The problem is solved for 24 hours duration (T) with timestep (Δt) of 15 minutes, and for simplicity the model is described for a generic instant t. The objective function aims at minimizing the operational costs over the simulation period, considering the power exchanges with the grid and with the chargers. The power exchanged with the grid on the AC side of the inverter accounts for both the import (P_t^{giAC}) and the export (P_t^{geAC}). The charging power of the chargers are P_t^{Ch1} for charger 1 (Ch1) and P_t^{Ch2} for charger 2 (Ch2). P_t^{geAC} is the sum of the power exported to the grid (P_t^{grid}) and the power consumed by the school (P_t^{Sc}).

$$\min \sum_{t \in T} (P_t^{giAC} * c_t^i + P_t^{grid} * c_t^e + P_t^{Sc} * c_t^{eSc} - (P_t^{Ch1} + P_t^{Ch2}) * c_t^{Ch}) * \Delta t$$

The prices are summarized in

Table 9. The export school price c_t^{eSc} is equal to the import price c_t^i, because if the export from the DC microgrid is sent to the school, the school does not import energy from the grid, saving the corresponding price. The export price c_t^e is instead equal to the market one, whereas c_t^{Ch} is the fee per kWh the user pay to charge the vehicle.

To ensure the power balance of the DC microgrid, the sum of all powers at the DC side of the grid inverter has to be equal to zero:

$$P_t^{Ch1} + P_t^{Ch2} - P_t^{PV} - \left(P_{1,t}^{bd} + P_{2,t}^{bd} + P_{3,t}^{bd} + P_{1,t}^{bc} + P_{2,t}^{bc} + P_{3,t}^{bc}\right) - P_t^{gi} - P_t^{ge} = 0$$

where $P_{1/2/3,t}^{bd}$ the discharging is power of string 1, 2 or 3 and $P_{1/2/3,t}^{bc}$ is the charging power; P_t^{gi} and P_t^{ge} are the imported/exported powers at the DC side of the grid inverter and P_t^{PV} is the PV production.

Chargers' consumption and PV production profiles are provided a priori and always prioritized during the simulation. In order to ensure that the DC microgrid is operated as requested, the following constraints are introduced. First, the grid inverter constraints ensure that at each instant t:

1. If there is exchanged power with the grid, this should be either import or export;
2. The exchanged power is within the limits of the inverter capacity.

Second, the constraints on the single strings ensure that:

1. The string charges from the PV or the grid, or discharges towards the chargers or the grid;
2. Only one action is chosen between: charging/ discharging/ idling;
3. The string energy is constrained between max and min values throughout the entire T, and at the beginning and end of simulation the energy is fixed to the chosen values;
4. The string energy is equal to the energy at instant $t-1$ plus charging/ discharging power during Δt.

Third, the BESS constraints ensure that:

1. If there is consumption from the charger or production from the PV, one or more strings are available and ready to take the power in or out;
2. Only one string can import/export power from/to the grid at each instant.

Furthermore, imported/exported power at the grid inverter level, and charging/discharging power of the strings take the efficiency of the inverter and the string into account, reported in Figure 5 and Figure 8, respectively.

Figure 17 shows the PV production and the school and chargers' consumption during a summer day. PV production and school consumption profiles are based on the real measurements reported in Sections 2.3.2 and 2.4, respectively. The chargers' profiles are conservatively assumed by the authors, considering that the chargers are located close to a school on the Danish island of Bornholm.

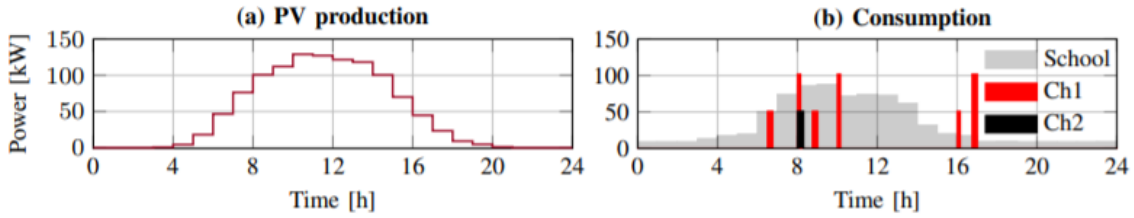

Figure 17: Subplot (a) provides the PV production during a summer day of the entire PV system; subplot (b) provides the consumption of the school, and the fictitious consumption of the 2 chargers [22].

When the DC microgrid is introduced, a third part of the PV plant (60 kWp) is connected to the DC bus, whereas the remaining 2/3 of PV is not changed. The DC microgrid is used to compensate, to the possible extent, the net load of the school, which is the sum of 1/3 of the school consumption and the import. If the PV contributes on an equal share to export and self-consumption, 1/3 PV in the DC microgrid is also a 33% reduction of export and self-consumption.

Figure 18 displays the result of the optimization model. Subplots (a), (b) and (c) provide the charging/discharging power and SOC of the three strings, respectively. Subplot (d) shows the exchanges of power at the inverter level, including the subdivision between export to the grid and export to the school.

It is relevant to observe that the PV production is enough to cover the chargers' consumption and to compensate for a share of the school net load. Indeed, no import is observed for the DC microgrid, and the entire export is used for the school net load (no export is directly going to the grid).

In order to compare the new system and the conservative solution for EV ultra-fast charger installations, Figure 19 shows the imported and exported power at the grid connection level in the two cases, whereas Table 10 provides the energy amounts. The DC microgrid decreases the export to the grid, due to the usage of 1/3 PV in the microgrid. Nevertheless, it also has a positive impact on the grid connection, as the import power request is 5 times smaller than in the conservative scenario. Indeed, the power request in the conservative scenario reaches a peak of 140 kW, whereas in the new system the maximum is only of 29 kW.

Table 10: Imported and exported energy during one day for the conservative and the new system solutions.

Energy, kWh/day	Conservative solution	New system
Import	208	132
Export	385	283

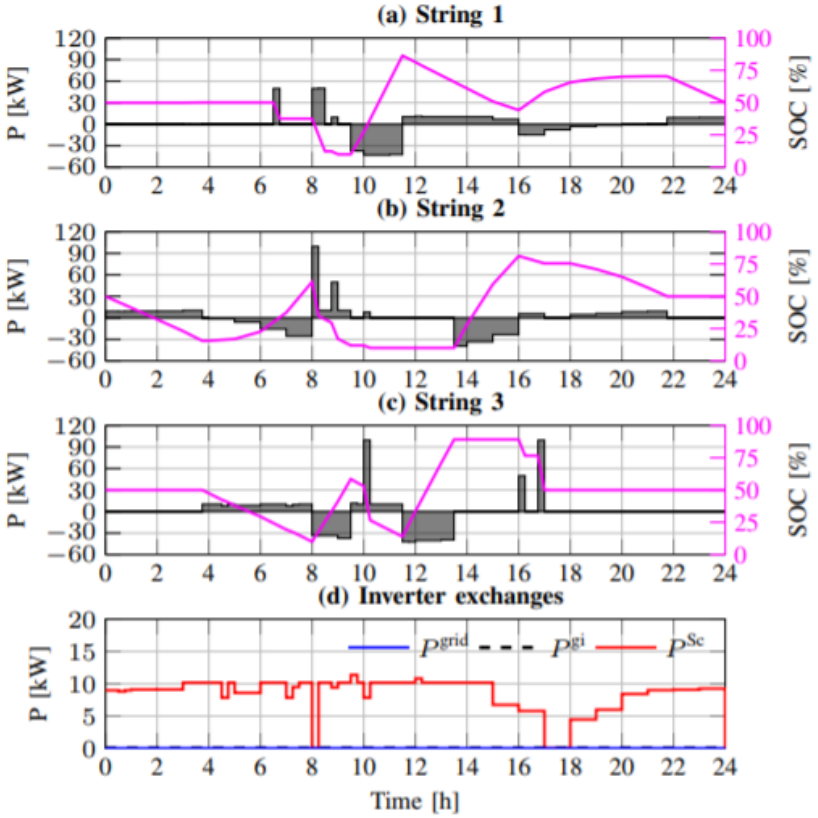

Figure 18. Subplots (a), (b) and (c) provide the power and SOC of strings 1, 2 and 3, respectively. Subplot (d) shows the exchanges of power at the grid inverter [22].

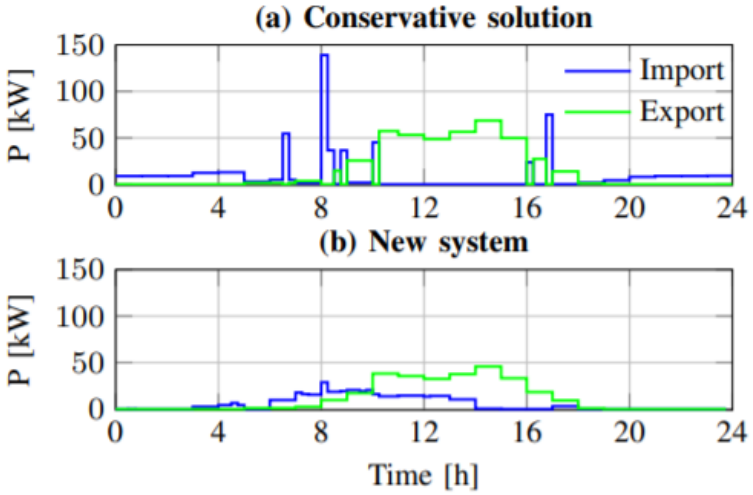

Figure 19: Comparison of grid exchanges, import and export, between the conservative and the new system solutions.

3.2 Battery management system

3.2.1 Control objectives

The novel battery technology of the BESS allows to re-arrange the connection scheme of the battery cells during operation. Figure 20 provides a graphical overview of how this reconfigurable design is achieved. Each cell is equipped with two semiconductor switches (MOSFETs). The switches are controlled by the battery management system (BMS) to either engage or bypass individual cells without interrupting the current path through the string. In the example shown in Figure 20, Cell 1 and Cell 27 are engaged, while Cell 2 is bypassed. The optimal cell configuration for each string is chosen according to two objectives:

1. To provide the required voltage and current levels for EV, PV system, and inverter.
2. To balance the state-of-charge (SOC) of the different cells within the same string and keep them within a certain tolerance band.

Hence, the BMS ensures safe operation of the whole battery while operating all cells according to their individual performance.

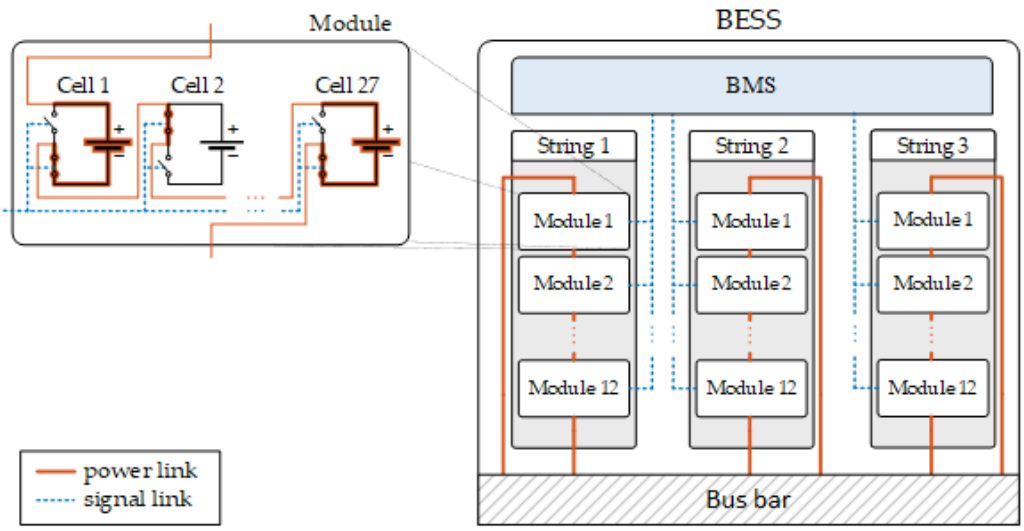

Figure 20: Schematic overview of how the reconfigurable design is achieved. The BMS is able to change the connection state of each individual cell by controlling semiconductor switches within the battery modules. Hence, the topology of each string can be adapted in a real-time fashion.

To test the reconfigurable design in a simulative environment, a mathematical model of the battery system was developed in Matlab & Simulink. The modelling approach for the battery strings is described in the following Section 3.2.2. The individual string models were coupled with models for PV system, EV, and inverter. This allowed us to verify, if the BMS can fulfill the above mentioned

objectives for each of these components. Sections 3.2.3, 3.2.4, and 3.2.5 summarize the obtained simulation results for the coupling with PV system, EV, and inverter, respectively.

3.2.2 BESS model

Each BESS string was modelled on cell level in order to capture the reconfigurable properties of the system. The electric behavior of the cell is formulated as a Thevenin equivalent, comprising an open-circuit voltage and a cell resistance, as shown in Figure 21. Hence, the cell voltage is dependent on the current flowing through the cell and is given by $V_{cell} = V_{oc,cell} - I_{cell} \cdot R_{cell}$.

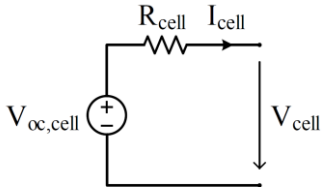

Figure 21: Cell equivalent circuit used to represent the electric behaviour of one single cell.

The values for open-circuit voltage and resistance have a dependency on the cell SOC. This dependency was experimentally determined in the laboratories of Nerve Smart Systems and is shown in Figure 22. As seen in the graphs, the cells in the developed battery model are only operated within SOC limits of 10% and 90% in order to prevent over- or undercharging.

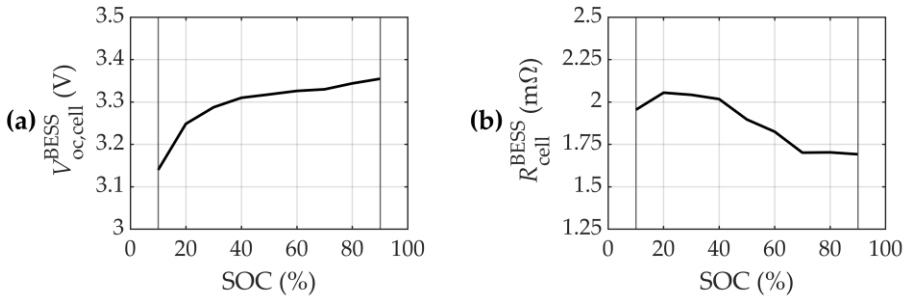

Figure 22: Cell characteristics of a 100Ah LFP cell. The graphs show the obtained SOC dependency at 25 °C for: (a) open-circuit voltage; (b) cell resistance.

The SOC changes when an electric current is applied to the respective cell, and is monitored by the BMS. Based on the individual states of all cells and the requirements for voltage and current of the battery string, the BMS decides in real-time on the optimal cell configuration. In our paper [13], we extensively describe the controlling algorithm that is responsible for the decision making process.

The electric behavior of the battery string is given by the sum of all cell models, as indicated in Figure 20.

3.2.3 PV scenario

When operating PV systems, commonly a power converter is used to apply a technique called Maximum Power Point Tracking (MPPT) to maximize power extraction under all conditions. When the irradiance changes, e.g. because of clouds, the converter must change the voltage at the PV module terminals to find the best operating point (optimal voltage) for the new condition. This is commonly done through a method called “perturb and observe”, where the voltage is adjusted while measuring the output power. If the power increases, the inverter applies further adjustments in that direction until the power reaches a steady state. Since the present setup has no power converters between the battery string and the PV system, the BMS must adjust the number of engaged cells during operation to achieve the same functionality. This was tested in a simulative environment by coupling the string model in Matlab & Simulink with a PV model. The PV model was developed using the information of the PV modules [15]. As input for the PV model, irradiance measurements from Roskilde, Denmark, were used since no historical data of Bornholm were available. For the simulation, the measurements from 11th August 2019 were chosen as they contain strong fluctuations in irradiation which is generally more challenging for the MPPT function. The goal of the simulations was to assess if a reconfigurable battery can be used to perform MPPT for a PV system. The battery string was initialized with a starting SOC of 25% and an allowed SOC difference between the highest and lowest cell SOC of 5%. The work is reported in [23].

Figure 23 provides an overview of the obtained simulation results. The subplots show the irradiance profile, the voltage at the PV system terminals, the extracted power, and the maximum and minimum cell SOC within the connected battery string, respectively.

As seen from subfigure d), the string SOC increases from its initial SOC as it is getting charged by the PV system. When the string SOC reaches 95%, the SOC is reset to 25% which imitates the process of switching the current string with another string with 25% SOC. The difference between the maximum and minimum cell SOC was 5% throughout the whole simulation. Hence, the BMS was capable of balancing the SOC with performing MPPT. In their respective plots, voltage and power are compared to the ideal/optimal values that would lead to the maximum energy extraction.

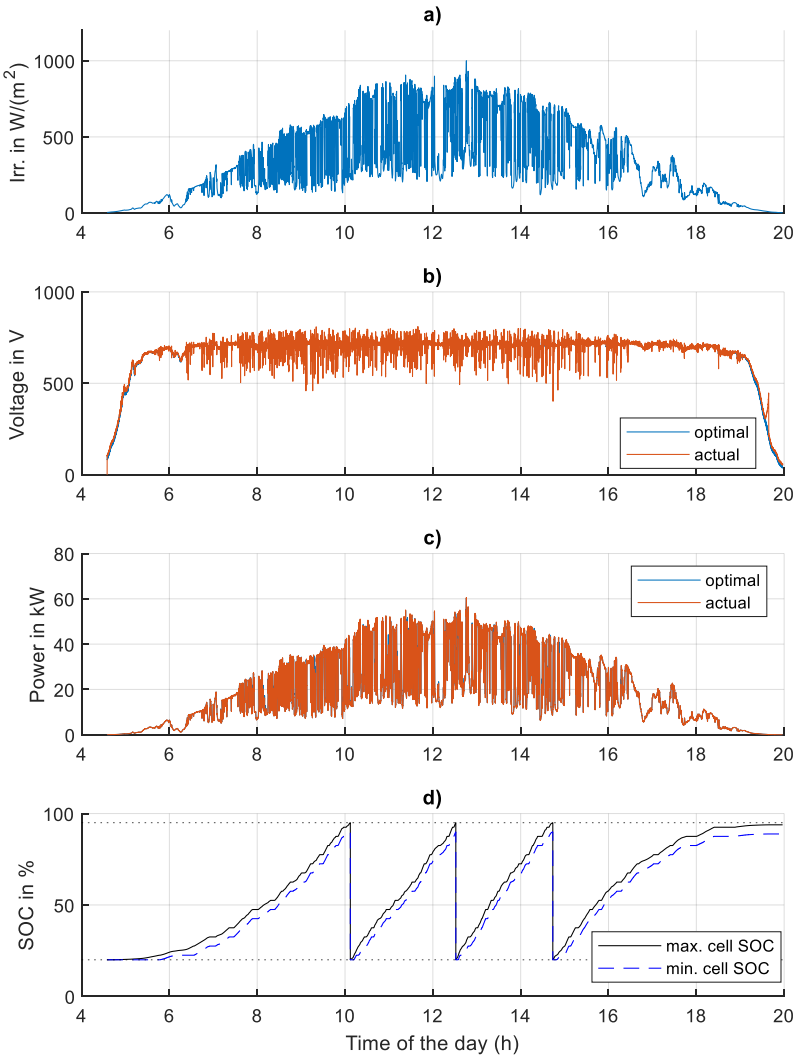

Figure 23: Simulation result of a reconfigurable battery string performing PV MPPT for a whole day. a) Irradiance measurement as input to the model; b) Comparison of optimal and actual voltage applied by the string; c) Comparison of optimal and actual power extraction; d) Maximum and minimum cell SOC within the battery string.

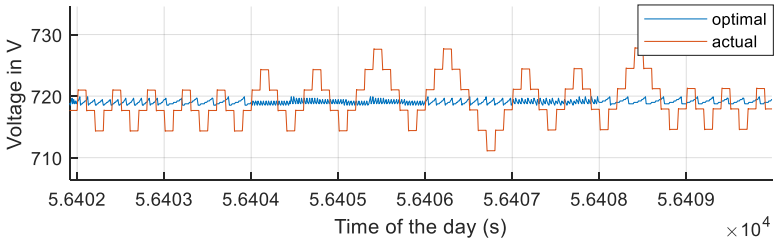

Figure 24: Close view of voltage control by reconfigurable battery string performing PV MPPT.

Furthermore, when the irradiance changes rapidly, the MPPT algorithm needs time to find the new voltage setpoint. Figure 25 gives an example of voltage and power progressions for changing irradiance levels. It can be seen that for rapid changes in the irradiance, the MPPT control needs a few seconds to find the optimal voltage again. During the times when the difference between optimal and actual voltage is significant, the actual power is lower than the optimal/maximum power output that could be achieved for this irradiance level. The accumulated difference between actual and optimal power defines the efficiency of the MPPT control. For the performed simulation of one day, the battery was extracting 284.03 kWh from the PV system. The maximum achievable energy output was 285.99 kWh, leading to an MPPT efficiency of 99.32%.

All in all, the simulation results showed that a reconfigurable battery is able to perform MPPT control for a PV system with a high efficiency, without the need for a power converter. During operation, the BMS is able to maintain balanced cell charge levels.

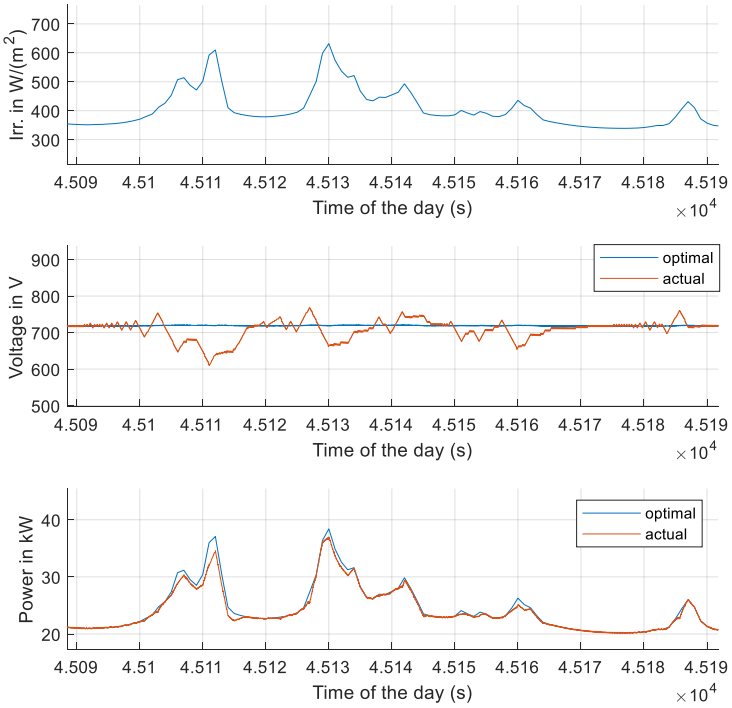

Figure 25: Performance of MPPT control during fast changes in irradiance level.

3.2.4 EV scenario

The aim of the EV scenario was to verify, whether the approach of adapting the cell configuration is suitable for controlling the power transfer to an EV. The vehicle considered in the investigation is the Nissan Leaf 2018 with CHAdeMO charging method, as we have in-depth knowledge of this vehicle from previous research activities. It is noteworthy, that the system installed on Bornholm is

equipped with CCS chargers which means that CHAdeMO vehicles cannot charge there. However, the simulation results have general validity, as both charging methods are summarized in charging standard IEC61851—Parts 23 and 24. Part 23 describes the technical specifications for DC electric charging stations [27], while Part 24 focuses on the digital communication between station and EV [28]. The standard was consulted to model the behavior of the EV and to later assess whether the BESS could meet the charging request with sufficient accuracy.

For the simulation, String 1 of the BESS was coupled with the model of the Nissan Leaf. For a detailed description of the EV model we refer to [13]. In the BMS, the allowed SOC band for the cells in String 1 was set to 5%. Hence, the controlling algorithm had to ensure that the SOC difference between the highest- and the lowest-charged cell did not exceed this value. At the beginning of the simulation, the initial SOC of the individual cells in String 1 were generated randomly with a uniform probability distribution within the limits of 85% and 90%. The SOC of the EV battery was set to an initial value of 0%.

Figure 26 provides an overview of the progressions of voltage, current, and SOC during the simulated EV fast charging procedure. At t = 0 s, the EV started its charging request and the power transfer was initiated. The charging procedure can be divided into two stages. During the constant current stage, the charging current was kept at its maximum while the voltage was increasing from its initial value of 290 V to the maximum EV battery voltage of 405 V. During this stage, the vehicle SOC was increasing linearly from 0% to 83% within 50 min. At this point in time, the voltage applied by String 1 reached the maximum EV battery voltage which initiated the constant voltage stage. Here, the voltage was held at its maximum while the charging current declined. As a result, the EV SOC was increasing more slowly. After 70 min the EV reached a final SOC of 97% and the charging process was terminated. Due to the energy transfer to the EV, the overall charge level of String 1 decreased to an average value of 47%. Throughout the charging procedure, the BESS was able to keep the cells within the allowed SOC range of 5%, as seen by the progressions of maximum and minimum cell SOC. During the simulated fast charging process, a total energy amount of 41.09kWh was transferred from the BESS to the vehicle. Of this energy, 39.08 kWh could be stored in the EV battery, while 2.01 kWh were dissipated as heat. Thus, the estimated EV efficiency is 95.1%. To provide the required energy, 44.06 kWh were extracted from the cells in String 1. Consequently, the BESS efficiency during the EV charging process was 93.3%. The losses of the BESS can be divided into losses generated by cells and MOSFETs which amount to 2438 Wh and 536 Wh, respectively. Hence, the energy loss caused by the MOSFETs corresponds to 1.2% of the total energy extracted from String 1. Since the proposed battery design does not require a DC-DC converter for controlling the EV charging process, the additional losses caused by the MOSFETs can be compared against the saved converter losses. The achieved efficiency of DC-DC converters used in fast charging stations lies around 96–98% [13], [14]. Hence, the proposed BESS design has a competitive efficiency compared to a battery buffered fast charging station with power converter.

In Figure 26(b), the current request sent by the EV is compared to the actual charging current provided by the BESS. The light blue lines indicate the allowed tolerance band defined in charging

standard IEC 61851. As seen in the plot, the BESS was able to follow the request during both charging stages. This demonstrates the general capability of controlling the charging current by adapting the number of engaged cells, without the need of any power converter. During the constant current stage, the EV request was met with sufficient accuracy. However, deviations between reference and actual current are visible. Towards the end of the constant voltage charging stage, these deviations occasionally exceeded the tolerance band. In [14], we discuss in detail the origin of the mentioned deviations and propose complementary measures to achieve a suitable current control during all phases of the charging process.

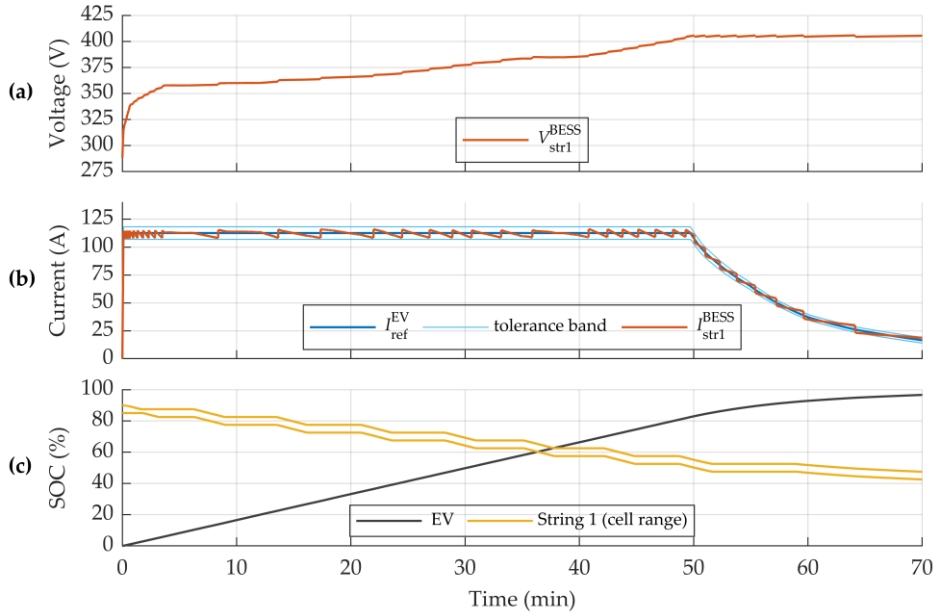

Figure 26: Simulation results of the EV fast charging process: (a) charging voltage; (b) comparison of actual charging current and reference current requested by EV; (c) SOC of EV and String 1. For String 1, the progressions of the highest and the lowest cell SOC are shown.

Since the charging process is controlled by adapting the number of engaged cells, the cell SOC across the String will start to vary with the start of the power transfer. Engaged cells will experience a change in their SOC, while the SOC of bypassed cells remains constant. One of the objectives of the BMS is to ensure that the SOC difference between cells will stay within a defined tolerance band. In the present case study, this band was set to 5%. Figure 27 demonstrates the principle according to which the BMS balanced the string SOC during the power transfer from BESS to EV. The power progression is given as the product of voltage and current at the connection point to the EV. Consequently, the current deviations seen in Figure 26 are also reflected in the power progression. During constant current charging, the power keeps increasing due to the rise in the voltage. The maximum power value of 46.8 kW is reached at the end of this charging phase where

both voltage and current are maximum. During constant voltage charging, the power declines due to the decreasing charging current. It is noteworthy that the maximum charging power in the performed simulation is limited by the considered vehicle (Nissan Leaf 2018). The BESS could generally provide charging power of up to 350 kW with one EV connected, or 175kW with two EVs connected, as reported in Section 2.1.

In the SOC graph in Figure 27, each line represents the SOC progression of one single cell which allows to demonstrate the cell balancing method. The line colour indicates in which module the cell is located. As defined in the case study, the cells in the battery string have a random initial SOC between 85% and 90%. The connection state of the cells can be identified through their individual SOC trend. Due to the discharging process, the SOC of an engaged cell is declining while the SOC of a bypassed cell remains constant. To maintain a balanced charge level across the string, the controlling algorithm makes sure that newly engaged cells are always the ones with the highest SOC. These cells remain engaged until their SOC reaches the lower limit of the defined SOC band. At this point, they will get bypassed and replaced by cells from the upper limit of the SOC band. Bypassed cells remain disconnected until they become the cells with the highest SOC due to the discharging of other cells. Hence, the controlling algorithm utilizes the flexibility within the SOC band to minimize the number of switching events per cell. The behaviour described above leads to the distinctive SOC profile seen in Figure 27. The progression of the band can be described as a stepwise decrease, where sections with linear decline are followed by plateaus with constant SOC levels. The plateaus occur every 5%, which corresponds to the width of the SOC band. During the constant voltage stage, the SOC is decreasing slower due to the declining charging power. At the end of the simulation, String 1 reached an average charge level of 47%.

All in all, the results suggest that a reconfigurable battery is generally able to control the power transfer to an EV without the need of a DC-DC converter interconnected between the two units. By adapting the number of engaged cells in a real-time fashion, the BESS could fulfil the EV request with sufficient accuracy for most of the charging process. However, the switching of cells causes voltage steps that can potentially lead to variations in the charging current. The demonstration project on Bornholm will offer the unique opportunity to verify this behaviour in field tests.

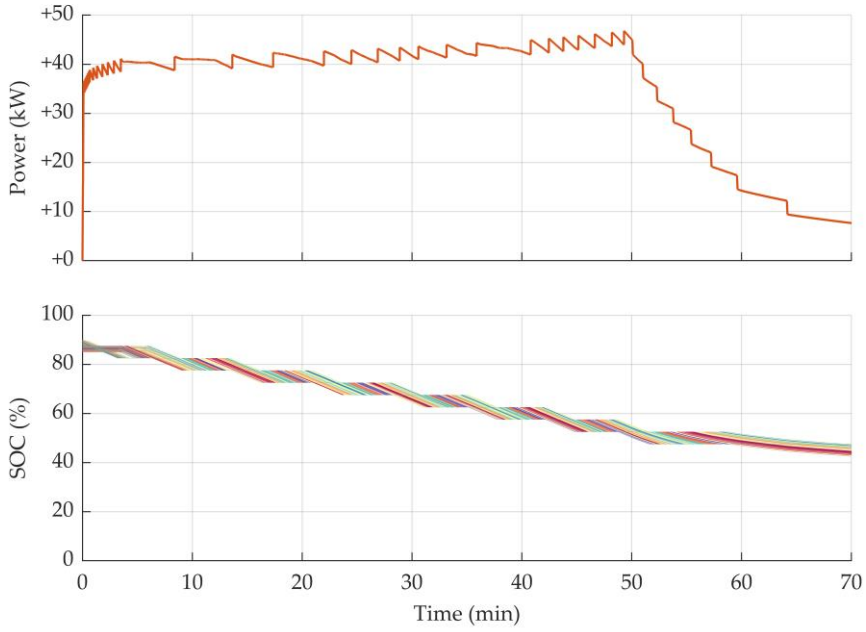

Figure 27: Simulated progressions of power (top plot) and SOC (bottom plot) for the battery string during the EV fast charging process. In the bottom plot, each line represents the SOC progression of one single cell. Line colours indicate cells of the same module.

3.2.5 Inverter scenario

The goal of the inverter scenario is to assess, how the reconfigurable battery can be operated when being coupled with a controllable power source, such as an inverter. The two units are coordinated in a way that the battery is responsible for controlling the DC link voltage, while the inverter is controlling the power flow to and from the grid according to its setpoint. The inverter is modelled as an ideal power source that, depending on the DC link voltage, supplies the required current to meet the reference power. The case study was designed to verify how the reconfigurable design is capable of regaining and maintaining balanced cell states, when being recharged through the grid-connected inverter. For the simulation, the setpoint for the inverter was set to a constant value of -22 kW. It should be noted that the sign convention for the reference power is the same as for the BESS string current: negative power values correspond to charging, thus leading to an increase of the string SOC. As for the EV charging scenario, the maximum allowed SOC difference across the string was set to 5%. The initial SOC of the individual cells was generated randomly with a uniform probability distribution between 10% and 30%, thus intentionally exceeding the tolerance band. This allows for the verification of whether the BMS is able to bring the cell SOC differences back into the defined SOC band during the recharging process. The simulation result is presented in Figure 28.

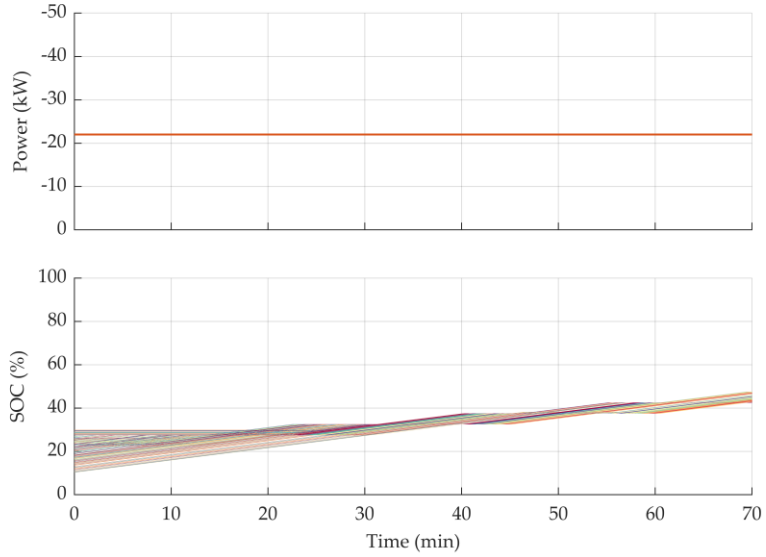

Figure 28: Simulated progressions of power (top plot) and SOC (bottom plot) for the battery string during the recharging process through the grid-connected inverter. In the bottom plot, each line represents the SOC progression of one single cell. Line colours indicate cells of the same module.

As seen in the SOC subplot, the individual cells were initialized with deviating cell SOCs between 10% and 30%. The controlling algorithm is pursuing balanced cell states by prioritizing cells with lower SOC values when deciding which cells to engage. Consequently, the SOC of low-charged cells is increasing while cells with a high SOC stay at their initial value. Hence, the controlling algorithm is "lacing" together the cell SOC across the string and bringing them back into the defined 5% band. From this point, the overall string SOC progression follows the same step-like characteristic seen for the EV charging case, but with increasing trend. After a simulation time of 70 min, the battery string reached an average charge level of 44%. The total energy amount provided by the grid-connected inverter was 25.67 kWh. From this value, 25.08 kWh could be stored in the battery string. Consequently, the efficiency for recharging was 97.7 %. The losses caused by cell resistances and MOSFETs were 524Wh and 63 Wh, respectively. Hence, the energy losses caused by the MOSFETs corresponds to 0.25% of the total energy provided by the grid-connected inverter. All in all, the results demonstrate that the reconfigurable design enables the battery to both regain and maintain a balanced SOC of cells of the same string.

4 CONCLUSIONS

This deliverable D4.8 gathers key information on the design of the DC microgrid as well as key results and main conclusions of the simulation studies performed in the Use Case 4. The results of the studies covered in the deliverable are summarized as follows:

1. All three energy management strategies tested during the simulation of the system performing fast charging at 9 operation scenarios comprised of 3 different PV production conditions and 3 different EV charging frequencies meet the objectives of the EMS and the energy components of the system, though with different performance. However, in the case of an extreme operation scenario combining low PV production and extremely high number and frequency of EV charging events (5 subsequently connecting 5 EVs per charger over the same time) the EV charging requirement could be fulfilled only partially. Herewith, charging maximum 3 EVs in a row by each charger could be achieved under condition of prioritizing the EV charging objectives over the PV harvesting objective, leaving the PV system disconnected. Moreover, the initial SOC of the BESS before the first EV charging should be not lower than 90%. It is worth mentioning here that the EV charging from the grid was not considered.
2. The PV production of the 61 kW PV system connected to the battery-based high-power charging station is enough to cover the consumption of the EV chargers performing ultra-fast charging and to compensate for a share of the school net load. Herewith, the import power request of the investigated system is up to 5 times smaller in amplitude than for the alternative conservative solution (29 kW versus 140 kW in peak).
3. The reconfigurable battery can be used to perform MPPT for a PV system with a high efficiency, without the need for a power converter. During operation, the BMS is able to maintain balanced cell charge levels. The maximum achievable energy output was 285.99 kWh, leading to an MPPT efficiency of 99.32%.
4. The reconfigurable battery is generally able to control the power transfer to an EV without the need of a DC-DC converter between the two units. By adapting the number of engaged cells in a real-time fashion, the BESS could fulfil the EV request with sufficient accuracy for most of the charging process. However, the switching of cells causes voltage steps that can potentially lead to variations in the charging current. The proposed BESS design has a competitive efficiency compared to a battery buffered fast charging station with a DC-DC converter.
5. The reconfigurable design is capable of regaining and maintaining balanced cell states, when being recharged through the grid-connected inverter. In a simulation scenario with initially unbalanced cell states, the BMS was able to bring the cell SOC differences back into the defined SOC band during the recharging process. The efficiency for recharging was 97.7 %.

The results of the simulation-based studies allow to make preliminary conclusions on several Key Performance Goals formulated for the Use Case 4 in [10].

1. Reduction in power need from the AC grid to supply EV fast chargers – confirmed by results presented in 2.2.2 and 2.2.3.
2. Increase of the energy self-sufficiency of Campus Bornholm through the PV system – confirmed by results presented in 2.2.3. A 33% reduction of export and self-consumption could be achieved.
3. Reduction of energy losses due to the reduction of conversion stages – confirmed by results presented in 2.3.4.
4. Proof of concept of hybrid AC-DC grids – confirmed by all the studies presented. Will be further investigated during the foreseen demonstration activities.

Provision of multiple ancillary services via smart management of the three storage strings and Reduction of power electronics investment cost have not been tested through simulations will be further investigated during the foreseen demonstration activities.

D4.8 concludes, together with D4.9 (Bornholm Lighthouse Use Case-5 report) [32], the simulation activities in the task T4.3 (Bornholm Lighthouse demonstration preparatory activities) of the INSULAE project.

REFERENCES

[1] M. Marinelli et al., "Electric Vehicles Demonstration Projects - An Overview Across Europe," 2020 55th International Universities Power Engineering Conference (UPEC), Turin, Italy, 2020.

[2] A. Thingvad, P.B. Andersen, T. Unterluggauer, C. Træholt, M. Marinelli, "Electrification of Personal Vehicle Travels in Cities - Quantifying the Public Charging Demand," e-transportation. In press.

[3] L. Calearo, M. Marinelli, C. Ziras, "A Review of Data Sources for Electric Vehicle Integration Studies," Renewable & Sustainable Energy Reviews. Under review.

[4] T. Gabderakhmanova, M. Marinelli, "A Review of Demonstration Activities in Multi-Energy Systems on European Islands," Energy. Under review.

[5] I. B. Sperstad et al., "Cost-Benefit Analysis of Battery Energy Storage in Electric Power Grids: Research and Practices," Innovative Smart Grid Technologies (ISGT Europe), 2020 IEEE PES International Conference and Exhibition on, pp. 1-5, The Hague, 25-28 Oct. 2020.

[6] P. Divshali et al, "Battery Storage Demonstration Projects An overview across Europe," ISGT Europe 2021. Under review

[7] Z. M. Pinter, D. Papageorgiou, G. Rohde, M. Marinelli, C. Træholt, "Review of Control Algorithms for Reconfigurable Battery Systems with an Industrial Example," UPEC 2021. Under review

[8] Nerve Smart Systems ApS official website. [Online]. Available: https://nervesmartsystems.com/

[9] T. Gabderakhmanova, J. Engelhardt, J.M. Zepter, Th. Meier Sørensen, K. Boesgaard, H. H. Ipsen, M. Marinelli, "Demonstrations of DC Microgrid and Virtual Power Plant Technologies on the Danish Island of Bornholm," Universities Power Engineering Conference (UPEC), 2020 Proceedings of the 55th International, pp. 1–6, Torino, 1–4 Sep. 2020. https://doi.org/10.1109/UPEC49904.2020.9209853

[10] T. Gabderakhmanova, M. Marinelli, J.M. Zepter, J. Engelhardt, T. Meier Sørensen, A.S. Poulsen, H.H. Ipsen, T. Jørgensen, K.M. Andreasen, K. Boesgaard, N. Schwartz, "Bornholm Lighthouse Interventions Equipment Detailed Engineering," Insulae D4.11. WP4: Modelling, simulation, engineering and equipment development for the Lighthouse demonstration, Oct. 2020.

[11] C. Ziras, L. Calearo, M. Marinelli, "The Effect of Net Metering Methods on Prosumer Energy Settlements," Sustainable Energy, Grids and Networks. Under review.

[12] L. Calearo, C. Ziras, K. Sevdari, M. Marinelli, "Comparison of Smart Charging and Battery Energy Storage System for a PV Prosumer with an EV," ISGT Europe 2021. Under review.

[13] J. Engelhardt, J. M. Zepter, T. Gabderakhmanova, G. Rohde, and M. Marinelli, "Double-String Battery System with Reconfigurable Cell Topology Operated as a Fast Charging Station for Electric Vehicles," Energies, vol. 14, no. 9, p. 2414, 2021.

[14] J. Engelhardt, T. Gabderakhmanova, G. Rohde, M. Marinelli, "Reconfigurable Stationary Battery with Adaptive Cell Switching for Electric Vehicle Fast-Charging. In Proceedings of the 2020 55th International Universities Power Engineering Conference (UPEC), Turin, Italy, 1–4 September 2020; pp. 1–6.

[15] Trina TSM-265-DC05A.05 PV modules datasheet http://www.solardesigntool.com/components/module-panel-solar/Trina-Solar/2505/TSM-265-DC05A.05/specification-data-sheet.html

[16] SMA Tripower 60 kW inverter data sheet https://files.sma.de/dl/25977/STP60-10-DEN1818-V26web.pdf

[17] Bilstatistik Bornholm 2018. [Online]. Available: https://www.bilstatistik.dk/

[18] X. H. Sun, T. Yamamoto, and T. Morikawa, "Fast-Charging Station Choice Behaviour Among Battery Electric Vehicle Users," Transportation Research Part D: Transport and Environment, vol. 46, pp. 26–39, 2016.

[19] Live data measurements. DTU Lyngby campus building 325. 22 kW DC charger. [Online]. Available: https://evbe.elektro.dtu.dk/plot.html?id=ly325.util.evse.06

[20] Converdan AFE333KAC inverter datasheet. https://www.converdan.com/products/converters/afe333kac/; accessed on 10.06.2021.

[21] J. Gejl Lage, "Design of Energy Management Strategies for a Reconfigurable Battery System Coupled with an Electric Vehicle Fast Charger and Photovoltaics," Master thesis in electrical engineering, DTU, Jun 2021

[22] L. Calearo, M. Agostini, J. Engelhardt, M. Coppo, R. Turri, M. Marinelli, "Optimal Management of a Reconfigurable BESS to Reduce EV Ultra-Fast Charging Grid Impact", Under review.

[23] S. Schmidt Petræus, A. Thestrup Valgreen, "Performance Characterisation and Dynamical Behaviour of a Reconfigurable Battery System", Master thesis in electrical engineering, DTU, June 2021.

[24] M. Marinelli, J. Engelhardt, J. M. Zepter, T. Gabderakhmanova, "Bornholm Lighthouse Energy System Models," Insulae D4.10. WP4: Modelling, simulation, engineering and equipment development for the Lighthouse demonstration, Apr. 2020.

[25] K. Knezović et al. 2017. Supporting Involvement of Electric Vehicles in Distribution Grids: Lowering the Barriers for a Proactive Integration. Energy 134: 458 – 468. https://doi.org/10.1016/j.energy.2017.06.075

[26] INSULAE –Part B document. Ref. A (2019) 7621742 - 11/12/2019.

[27] International Electrotechnical Commission (IEC). *Electric Vehicle Conductive Charging System—Part 23: DC Electric Vehicle Charging Station*; International Standard DS/EN 61851-23:2014/AC:2016; IEC: Geneva, Switzerland, 2016.

[28] International Electrotechnical Commission (IEC). *Electric Vehicle Conductive Charging System—Part 24: Digital Communication between a DC EV Charging Station and an Electric Vehicle for Control of DC Charging*; International Standard DS/EN 61851-24:2014; IEC: Geneva, Switzerland, 2014.

[29] W. Lee, J. Kim, J. Lee, I. Lee. Design of an Isolated DC/DC Topology with High Efficiency of Over 97% for EV Fast Chargers. IEEE Trans. Veh. Technol. 2019, 68, 11725–11737.

[30] F. Hoffmann, T. Pereira, M. Liserre. Isolated DC/DC Multimode Converter with Energy Storage Integration for Charging Stations. In Proceedings of the 2020 IEEE Energy Conversion Congress and Exposition (ECCE), Detroit, MI, USA, 11–15 October 2020; pp. 633–640.

[31] L. Calearo, A. Thingvad, M. Marinelli. Validation of a Lumped Battery Model for Electric Vehicle Degradation Studies. Manuscript submitted for publication.

[32] J.M. Zepter et al., "Bornholm Lighthouse Use Case-5 report", Insulae D4.9. WP4: Modelling, simulation, engineering and equipment development for the Lighthouse demonstration, June 2021.